The NOW regional coupled model: Application to the tropical Indian Ocean climate and tropical cyclone activity

Guillaume Samson, Sébastien Masson, Matthieu Lengaigne, Madhavan Girijakumari Keerthi, Jérôme Vialard, Stéphane Pous, Gurvan Madec, Nicolas C. Jourdain, Swen Jullien, Christophe E. Menkès, et al.

AGU PUBLICATIONS

Journal of Advances in Modeling Earth Systems

RESEARCH ARTICLE

10.1002/2014MS000324

Key Points:
- Application of a new coupled regional climate model to the tropical Indian Ocean
- Sensitivity to convection schemes from intraseasonal to interannual time scales
- Role of ENSO for triggering the Indian Ocean Dipole

Correspondence to:
G. Samson,
guillaume.samson@gmail.com

Citation:
Samson, G., S. Masson, M. Lengaigne, M. G. Keerthi, J. Vialard, S. Pous, G. Madec, N. C. Jourdain, S. Jullien, C. Menkes, and P. Marchesiello (2014), The NOW regional coupled model: Application to the tropical Indian Ocean climate and tropical cyclone activity, *J. Adv. Model. Earth Syst.*, *6*, 700–722, doi:10.1002/2014MS000324.

Received 14 MAR 2014
Accepted 2 MAY 2014
Accepted article online 10 MAY 2014
Published online 5 AUG 2014

The NOW regional coupled model: Application to the tropical Indian Ocean climate and tropical cyclone activity

G. Samson[1,2], S. Masson[1], M. Lengaigne[1,3], M. G. Keerthi[3], J. Vialard[1], S. Pous[1,4], G. Madec[1], N. C. Jourdain[5,6], S. Jullien[1,2], C. Menkes[1], and P. Marchesiello[2]

[1]LOCEAN Laboratory, Sorbonne Universités (UPMC, Univ Paris 06)-CNRS-IRD-MNHN, IPSL, Paris, France, [2]Laboratoire d'Etudes en Géophysique et Océanographie Spatiales, IRD/CNES/CNRS/UPS, Toulouses, France, [3]Indo-French Cell for Water Sciences, IISc-NIO-IITM-IRD Joint International Laboratory, NIO, Goa, India, [4]LMI ICEMASA, IRD, Department of Oceanography, University of Cape Town, Cape Town, South Africa, [5]Laboratoire de Glaciologie et Géophysique de l'Environnement, CNRS, Grenoble, France, [6]Climate Change Research Centre, University of New South Wales, Sydney, Australia

Abstract This paper presents the NOW regional coupled ocean-atmosphere model built from the NEMO ocean and WRF atmospheric numerical models. This model is applied to the tropical Indian Ocean, with the oceanic and atmospheric components sharing a common 1/4° horizontal grid. Long experiments are performed over the 1990–2009 period using the Betts-Miller-Janjic (BMJ) and Kain-Fritsch (KF) cumulus parameterizations. Both simulations produce a realistic distribution of seasonal rainfall and a realistic northward seasonal migration of monsoon rainfall over the Indian subcontinent. At subseasonal time scales, the model reasonably reproduces summer monsoon active and break phases, although with underestimated rainfall and surface wind signals. Its relatively high resolution results in realistic spatial and seasonal distributions of tropical cyclones, but it fails to reproduce the strongest observed cyclone categories. At interannual time scales, the model reproduces the observed variability associated with the Indian Ocean Dipole (IOD) and the delayed basin-wide warming/cooling induced by the El Niño Southern Oscillation (ENSO). The timing of IOD occurrence in the model generally matches that of the observed events, confirming the influence of ENSO on the IOD development (through the effect of lateral boundary conditions in our simulations). Although the KF and BMJ simulations share a lot in common, KF strongly overestimates rainfall at all time scales. KF also overestimates the number of simulated cyclones by a factor two, while simulating stronger events (up to 55 m s^{-1}) compared to BMJ (up to 40 m s^{-1}). These results could be related to an overly active cumulus parameterization in KF.

1. Introduction

The Indian Ocean (IO) is unique among the three tropical oceans for being bounded to the north by the Asian continent. The resulting summer land-sea temperature gradient promotes the development of a low-level cross-equatorial jet [*Findlater*, 1970] that transports moisture from the ocean toward the Asian continent, giving rise to the strongest monsoon on Earth. The anchoring of the rising branch of the Walker circulation over the maritime continent also prevents the formation of steady easterlies over the equatorial IO. This precludes the formation of a semipermanent upwelling in the eastern part of the basin, as in the Atlantic or Pacific oceans. Instead, upwelling occurs along the coasts of Oman and Somalia and at the southern tip of India [see *Schott et al.*, 2009, for an extensive review on IO climate system]. As a consequence of this absence of climatological upwelling, the eastern IO is very warm, and forms a non-negligible part of the Indo-Pacific warm pool. A large portion of the IO exhibits sea surface temperatures (SST) in excess of the 28.5°C threshold for deep atmospheric convection [*Graham and Barnett*, 1987]. As a result, small SST variations can induce a relatively large atmospheric response, hence facilitating very active air-sea interactions across a variety of time scales.

In addition to seasonal variations, the IO also exhibits clear interannual fluctuations. Some of these fluctuations are strongly influenced by the neighboring Pacific Ocean. The powerful climate fluctuations induced by the El Niño/Southern Oscillation (hereafter ENSO) [see *McPhaden et al.*, 2006] considerably alters the Walker circulation and surface temperatures in the IO [e.g., *Klein et al.*, 1999]: changes in cloud cover and wind patterns in response to El Niño events promote a basin-scale warming, which persists two seasons after the end of El Niño as a result of internal air-sea interactions within the tropical IO [*Du et al.*, 2009]. In

addition, ENSO is the strongest external control on interannual variations of the Asian monsoon (see review article by *Turner and Annamalai* [2012]), although that influence has weakened over the recent decades [*Krishna Kumar et al*., 1999]. The IO also exhibits an intrinsic mode of air-sea coupled variability [*Saji et al*., 1999; *Webster et al*., 1999], commonly referred to as the Indian Ocean Dipole (IOD). In its positive phase, this climate mode is associated with anomalous easterly winds in the central IO and cold SST anomalies off the west coasts of Java and Sumatra, intimately tight through a positive coupled feedback loop. IOD events have a tendency to be triggered by El Niño, which reduces convection and favors easterlies over the IO, but they can also occur independently [*Annamalai et al*., 2003; *Yamagata et al*., 2004; *Izumo et al*., 2010].

The IO also displays a very clear subseasonal and synoptic variability. The monsoon itself does not occur as a continual downpour during the entire summer but rather as intraseasonal pulses, referred to as active and break periods [see *Goswami*, 2005 for a review]. Although atmospheric processes essentially drive these intraseasonal rainfall fluctuations, they promote very clear SST signatures in the northern IO [e.g., *Vecchi and Harrison*, 2002; *Vialard et al*., 2012], which may significantly affect the eastward and northward propagation of these atmospheric intraseasonal perturbations [e.g., *Bellon et al*., 2008; *Klingaman et al*., 2011]. The IO is also home to about 25% of the global tropical cyclone activity. TCs in the Bay of Bengal, if not the most intense, have catastrophic impacts, with 14 of the 20 deadliest TCs in the world history having occurred in that region [*Longshore*, 2009]. While TCs primarily arise from atmospheric processes, they are nonetheless strongly influenced by ocean-atmosphere interactions. The SST cooling under TCs [e.g., *Price*, 1981; *Vincent et al*., 2012; *Neetu et al*., 2012] indeed reduces the total enthalpy flux to the atmosphere [e.g., *Schade*, 2000; *Bender and Ginis*, 2000] and hence limits the cyclone intensification. Ocean-atmosphere interactions may therefore modulate climate variability over a wide range of time scales.

To date, the most widely used numerical tools to investigate these coupled processes in the IO are Coupled Ocean-atmosphere General Circulation Models (CGCMs). Numerous CGCM studies have addressed the role of coupled air-sea interactions on large-scale atmospheric modes in the IO such as the IOD [e.g., *Yamagata et al*., 2004; *Fisher et al*., 2005; *Behera et al*., 2006] or the Indian Summer monsoon [e.g., *Wu and Kirtman*, 2004; *Fu and Wang*, 2004; *Izumo et al*., 2008]. CGCMs usually have spatial resolutions that are too coarse to correctly represent the regional characteristics of the Asian monsoon [*Krishna Kumar et al*., 2005; *Wang et al*., 2005; *Sperber et al*., 2012] such as orographic features or the low pressure across India. Similarly, the coarse resolution only allows simulating cyclone-like vortices that share some TCs properties but with much lower intensities [e.g., *Bengtsson et al*., 1996; *Vitart et al*., 1997; *Camargo et al*., 2005], whose relevance to actual TC activity remains difficult to assess [*Camargo et al*., 2007]. Increasing CGCM horizontal resolution to 50–20 km improves the representation of TCs [e.g., *Zhao et al*., 2010; *Murakami and Wang*, 2010; *Strachan et al*., 2013; *Jourdain et al*., 2014] and of the Asian monsoon [e.g., *Kitoh and Kusunoki*, 2007; *Satoh et al*., 2012], but the high computational cost of those simulations limits the number of sensitivity experiments that can be used for calibrating the model parameterizations.

In light of their smaller requirement for computational resources, a cost-effective alternative for studying air-sea interactions at high horizontal resolution relies in the development of coupled Regional Climate Models (RCMs). RCMs are a powerful tool for dynamical downscaling of large-scale climate signals and for studies of the physical mechanisms that shape the observed climate features in a given region [see *Wang et al*., 2004 for a review]. These tools improve the simulated climate and meteorological features in the IO compared to coarser resolution CGCMs, including the Indian Summer monsoon [e.g., *Ratnam and Kumar*, 2005; *Mukhopadhyay et al*., 2010; *Lucas-Picher et al*., 2011] and TCs [*Landman et al*., 2005; *Knutson et al*., 2007; *Jourdain et al*., 2011; *Jullien et al*., 2014, among others].

Only a few attempts have been made at running long-term coupled ocean-atmosphere RCMs simulations to investigate the influence of air-sea coupling on the climate and mesoscale features in the IO. *Ratnam et al*. [2008] and *Samala et al*. [2013] used a regional coupled model over a limited number of summer seasons to evaluate the influence of air-sea interactions on the Indian summer monsoon. These two studies suggested that accounting for this coupling improves the simulation of the climatological as well as intraseasonal oscillations of the monsoon rainfall. To the authors' knowledge, *Seo et al*. [2008, 2009] are to date the only two studies that performed 12 year long simulations using a coupled RCM for the IO sector. These long simulations were used to investigate the effect of mesoscale ocean-atmosphere coupling on the Somalia upwelling region [*Seo et al*., 2008] and to demonstrate that the freshwater forcing in the northern

part of the IO plays an important role during boreal winter by affecting SST and coupled ocean-atmosphere interactions [*Seo et al*., 2009].

In the present paper, we describe a newly developed coupled atmosphere-ocean RCM, applied to the tropical IO sector. RCMs are sensitive to the parameterization of subgrid-scale precipitation processes that strongly influence the representation of the monsoon [e.g., *Ratnam and Kumar*, 2005; *Dash et al*., 2006; *Mukhopadhyay et al*., 2010; *Zou and Zhou*, 2011] and of TCs [*Srinivas et al*., 2003, 2013a; *Deshpande et al*., 2010]. We therefore ran two sets of 20 year long coupled experiments, each with a distinct convective parameterization. The main goal of the present paper is to assess the ability of those coupled RCM long-term simulations to represent the IO climate, with a focus on the seasonal cycle, intraseasonal, and interannual variability, and the main characteristics of TC climatology. The sensitivity of the IO climate and TC activity to the cumulus parameterization will also be discussed. The paper is organized as follows. Section 2 provides a description of the coupled model, experimental design, TC tracking method, and validation data sets. Sections 3–5, respectively, provide a validation of the model at seasonal, intraseasonal, and interannual time scales. Section 6 validates the simulated TC climatology, structure, and intensity. Discussion and conclusion follow in section 7.

2. Model, Experiments, and Data Sets

2.1. Coupled Model Components

Our regional coupled model NOW (for NEMO-OASIS3-WRF) couples state-of-art atmospheric (WRF) and oceanic (NEMO) models through the OASIS3 coupler [*Valcke*, 2013]. The NOW components can be precisely configured by using the multiple options offered with each model (physical parameterizations, numerical schemes, etc.). The model components and the main options used for this study are briefly described below.

The ocean component is based on the NEMO (Nucleus for European Modelling of the Ocean) modeling system. Vertical mixing is modeled with a prognostic turbulent kinetic energy scheme, with background vertical diffusion and viscosity of 10^{-5} m^2 s^{-1} and 10^{-4} m^2 s^{-1}, respectively [*Blanke and Delecluse*, 1993]. Additional subgrid-scale mixing parameterizations include a bi-Laplacian viscosity and an iso-neutral Laplacian diffusivity [*Lengaigne et al*., 2003]. A detailed description of this oceanic model can be found in *Madec* [2008].

The atmospheric component is the Weather Research and Forecasting (WRF) version 3.2, which solves compressible, nonhydrostatic Euler equations with the Advanced Research WRF (ARW) dynamical solver [*Skamarock and Klemp*, 2008]. This model is originally a mesoscale model developed by NCAR for case studies and short-range forecasts, but its efficient dynamical core and the large number of available physical parameterizations allow to use it for a wide range of applications with large domains and for long-term integrations. WRF has demonstrated good skills when used as an RCM over different regions [*Leung et al*. 2006]. The physical parameterizations used in the present configuration include the WRF single-moment six-class microphysics scheme WSM6 [*Hong and Lim*, 2006], the Goddard shortwave radiation scheme [*Chou and Suarez*, 1999], the Rapid Radiation Transfer Model (RRTM) for longwave radiation [*Mlawer et al*., 1997], the Yonsei University planetary boundary layer YSU [*Noh et al*., 2003] with Monin-Obukhov surface layer parameterization, and the four-layer Noah land surface model [*Chen et al*., 1996]. The drag parameterization over the ocean is based on the work of *Donelan et al*. [2004] and accounts for observed surface drag coefficient at strong winds, this dimensionless coefficient being bounded to a value of 2.34×10^{-3} for winds greater than 33 m s^{-1}.

In this study, we test the sensitivity of the regional coupled model to two different widely used parameterizations of subgrid-scale convection: the Betts-Miller-Janjic (BMJ) scheme [*Janjić*, 1994] and the Kain-Fritsch (KF) scheme [*Kain*, 2004]. These two schemes largely differ in their formulation. BMJ scheme is a moist convective adjustment scheme, where the thermodynamic profile is adjusted toward an observed reference profile in a quasi-equilibrium state. The scheme essentially removes the conditional instability in each grid column by relaxing the vertical profile of temperature and specific humidity toward the reference profile with a time scale of 1–2 h. The scheme gets triggered if a parcel becomes warmer than the environment, when lifted from the lower troposphere to a level above the cloud base, following the moist adiabatic. Activation of BMJ scheme at a particular grid point is mainly determined by thermodynamics, i.e., the presence

convective available potential energy (CAPE). Vertical motions can enhance the activation of the scheme by moistening the low levels and midlevels, but otherwise have no explicit influence. The BMJ scheme was initially developed for tropical areas [*Betts*, 1986]. *Janjić* [1994] introduced a moisture profile and a relaxation time, which depend on a parameter called "cloud efficiency" that characterizes the convective regime. The cloud efficiency is proportional to a nondimensional combination of the entropy change, precipitation and the mean temperature of the cloud. This scheme has been tuned over several years for precipitation forecasts over North America [*Janjić*, 2000].

The Kain-Fritsch scheme is designed to simulate a vertical rearrangement of mass that eliminates CAPE within a specified time interval (approximately 30 min) and is triggered based on the grid-resolved vertical motion [*Kain and Fritsch*, 1993]. This vertical motion (w) is used to calculate a temperature perturbation (scaled as $w^{1/3}$), which determines whether a parcel can overcome its convective inhibition. The updated Kain-Fritsch scheme implemented in WRF [*Kain*, 2004] allows shallow convection, includes a minimum entrainment rate to suppress widespread convection in marginally unstable, relatively dry environments, and has changes in the downdraft formulation. Downdrafts are formed from air in the layer at 150–200 hPa above cloud base, and detrain over a fairly deep layer below the cloud base. The downdraft mass flux is estimated as a function of the relative humidity and stability just above cloud base, but is no longer related to vertical wind shear. The surface convergence with the induced vertical motion has a much bigger impact on the KF convective parameterization than on the BMJ convective parameterization.

A previous study investigating TCs climatology and interannual variability in the South Pacific using a $1/4^\circ$ long-term WRF simulation [*Jourdain et al*., 2011] showed that these two schemes yielded the best results in terms of TC formation and large-scale conditions, with BMJ outperforming KF in their region of interest. In addition, the latest and most exhaustive study discussing the performance of WRF for tropical cyclone prediction in the Bay of Bengal [*Srinivas et al*., 2013b] shows that, at 9 km resolution, the KF scheme provides the best simulations for intensity and track prediction, giving higher convective warming with stronger vertical motions relative to the other tested cumulus schemes. *Vaidya and Singh* [2000], *Mukhopadhyay et al*. [2010], and *Srinivas et al*. [2013a] on the other hand illustrated that the BMJ scheme produces the most reasonable mean monsoon pattern, with realistic atmospheric flow, surface pressure, heating profiles, and moist instability.

These oceanic and atmospheric components are coupled trough OASIS3 [*Valcke et al*., 2013], a general coupler that allows efficiently exchanging two-dimensional fields between the atmospheric and oceanic components.

2.2. Coupled Model Configuration and Experiments

The ocean vertical grid has 46 levels, with a resolution ranging from 5 m at the surface to 250 m at the bottom. The atmospheric grid has 28 sigma levels, with a resolution of 30 m near the surface increasing up to 1.5 km at 50 hPa. The oceanic and atmospheric components use the same horizontal Arakawa-C grid, based on a Mercator projection at $1/4^\circ$ resolution. This intermediate resolution allows capturing to a certain extent oceanic and atmospheric mesoscale features, such as oceanic eddies and TCs. Thanks to the common ocean and atmosphere grids, the OASIS coupler directly exchanges surface fields between the models without any spatial interpolation. This presents two advantages: a reduced computational cost and an exact conservation of the exchanged quantities. The OASIS coupler exchanges averaged oceanic and atmospheric parameters asynchronously every hour in order to fully capture high-frequency air-sea interactions. The exchanged surface fields between the two models are the following: SST, wind stress, longwave and shortwave radiations, turbulent heat fluxes, precipitation, and evaporation.

The geographical domain of this coupled model extends from 25.5°E to 142.25°E and from 34.5°S to 26°N and covers the entire tropical and subtropical IO (Figure 1). The bathymetry and orography as well as the land-sea mask for both models are obtained from a smooth combination of the 2 min U.S. Geological Survey (USGS) topography and the General Bathymetric Chart of the Oceans (GEBCO) data over shelves. Land use categories are from the USGS 24-category data set.

WRF lateral boundaries conditions are prescribed from the European Centre for Medium-Range Weather Forecasts ERA-Interim 0.75° resolution reanalysis [*Dee et al*., 2011] at 6 hourly intervals. The oceanic portions of the eastern, northern, and southern boundaries of the ocean domain use radiative open boundary

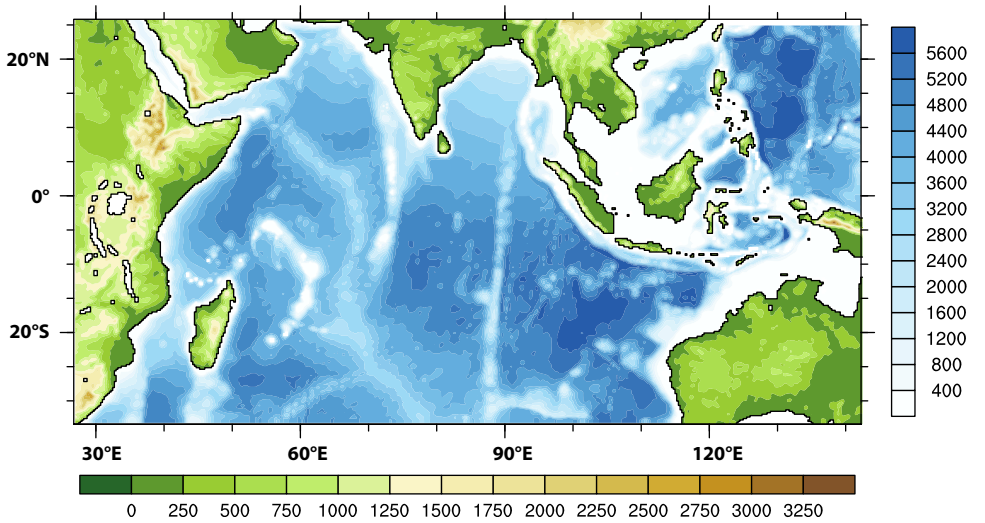

Figure 1. Bathymetry and orography of the NOW coupled model, derived from a smooth combination of the 2 min U.S. Geological Survey (USGS) topography and the General Bathymetric Chart of the Oceans (GEBCO) data over shelves.

conditions [*Treguier et al*., 2001] with a 150 days time scale relaxation to 5 day average velocities, temperature, and salinity from an interannual global $^1/_4^\circ$ simulation from which the IO sector ocean grid is extracted. This global simulation is a product of the DRAKKAR hierarchy of global configurations [*Brodeau et al*., 2010] forced with the Drakkar Forcing Set #4 (DFS4) described in *Brodeau et al*. [2010], and has been extensively validated in the Indo-Pacific regions [*Lengaigne et al*., 2011; *Keerthi et al*., 2012; *Nidheesh et al*., 2012]. No nudging is applied away from the boundaries, neither in the atmosphere nor in the ocean. A forced oceanic version of this regional configuration successfully reproduces IO oceanic variability at intraseasonal to interannual time scales [*Vialard et al*., 2011; *Kurian et al*., 2013; *Kumar et al*., 2014].

The initial condition on the 1st of January 1989 is provided from ERA-I reanalysis for the atmosphere and from the $^1/_4^\circ$ DRAKKAR simulation described above for the ocean. Two 21 years coupled simulations are performed with this setup over the 1989–2009 period, only differing by the convective parameterization they use BMJ for one experiment and KF for the other. The first year of both experiments is discarded, and the modeled and observed climatologies discussed in the following are computed over the 1990–2009 common period.

2.3. TCs Tracking Methodology

The method used to track TCs in the simulations has been developed by *Chauvin et al*. [2006] and adapted to WRF by *Jourdain et al*. [2011]. The following criteria are used to distinguish tropical cyclones from intense midlatitude systems at each time step:

1. 10 m wind $>$ 17.5 m/s associated with a local sea level pressure minimum.
2. 850 hPa vorticity $> 3 \times 10^{-4}$ s^{-1}.
3. 700–300 hPa mean temperature anomaly $>$ 1 K.

TCs temperature anomalies are calculated with respect to their large-scale environment: the TC region is defined as 3 radii of maximum wind (RMW) around the TC center while the environmental temperature is averaged between 6 and 9 RMW. Trajectories are then constructed by recursively detecting the closest neighboring grid points that meet all above criteria. If no matching point is identified, all criteria are relaxed except vorticity. This relaxation technique allows following TCs over land and during their extratropical transition, and avoids counting the same TC twice. Tracks shorter than 1 day are eliminated. The wind threshold was objectively determined following *Walsh et al*. [2007]. The vorticity and temperature thresholds were empirically calibrated from the analysis of the first year of simulation and from criteria used in similar numerical studies over the South-West Pacific [*Jourdain et al*., 2011; *Jullien et al*., 2014]. Two additional criteria originally used in *Jourdain et al*. [2011] (300 hPa temperature anomaly $>$ 850 hPa temperature anomaly

and 850 hPa tangential wind > 300 hPa tangential wind) were removed for sake of simplicity, as they do not alter TCs detections. TC statistics presented in section 6 are directly based on the results from this tracker.

2.4. Validation Data Sets

The model SST is validated against the 1/4° resolution optimally interpolated TMI (Tropical rainfall measuring mission-Microwave Instrument) data from Remote Sensing Systems (http://www.ssmi.com/sst/microwave_oi_sst_browse.html) over the 1992–2009 period. The model 10 m winds are compared to Quikscat/Seawinds scatterometer at 0.25° resolution processed by CERSAT (available from http://www.ifremer.fr/cersat/en/data/download/download.htm) over the 2000–2008 period. Model Sea Level anomalies (SLA) are compared to altimeter data produced by CLS Space Oceanography Division (available from http://www.jason.oceanobs.com/html/donnees/duacs/access_fr.html). Model precipitation rates are compared to the 1/4° TMI-AMSRE data set processed by NASA (available from http://www.ssmi.com/sst/microwave_oi_sst_data_description.html) over the 1998–2009 period. Other validation atmospheric fields such as the vertical wind shear, vorticity, and humidity are derived from the ERA-Interim reanalysis at 0.75° resolution [*Dee et al*., 2011]. TC statistics are validated against the WMO-IBTracs v3.1 global database [*Knapp et al*., 2010], that merges TC tracks and intensities data from the operational meteorological forecast centers.

We will compare the simulated wind and rainfall radial profiles to idealized profiles, which are based on a statistical fit to observed TC characteristics. Observationally based wind profiles are taken from the analytical formulation proposed by *Willoughby et al*. [2006]. In this formulation, the wind increases as a power of radius inside the eye and decays exponentially outside the eye with a smooth polynomial transition across the eyewall. Power law coefficients are fitted to 493 observed aircraft profiles from the Atlantic and Northeast Pacific region. Similarly, observationally based precipitation profiles are taken from *Tuleya et al*. [2007] who proposed a simple equation to represent the radial structure of rainfall profiles derived from 260 global TCs measured by the Tropical Rainfall Measuring Mission (TRMM).

3. Seasonal Cycle

Figure 2 shows the 10 m wind, sea level, SST, and precipitation boreal winter (December–March) climatology from observations and the two experiments. During this season, there is a sharp transition between the steady southeasterly trades south of 15°S and the south equatorial westerly, while the low-level northeast monsoon jet blows southwestward in the Arabian Sea (Figure 2a). The basin-scale sea level signals are largely the result of the integration of wind forcing (zonal wind at the equator and wind curl away from it), with some nonlocal effects due to planetary wave propagation [e.g., *McCreary et al*., 1993]. The pronounced downwelling observed at the southern tip of India (Figure 2a) is, for example, opposed to the effect of alongshore wind forcing. This signal is indeed the result of remote forcing from the Bay of Bengal, that has propagated counter clockwise along the coasts as a coastal Kelvin wave [e.g., *McCreary et al*., 1993]. This signal further expands northward along the western Indian coast as downwelling coastal Kelvin waves, and westward into the Arabian Sea as a Rossby wave. The shallow thermocline along eastern and northern rim of the Bay of Bengal is also the result of remote forcing, this time generated by equatorial westerlies in October–December that yields an equatorial upwelling Kelvin wave that propagates into the Bay as a coastal Kelvin wave. The southward wind in the Arabian Sea brings cold continental air that drives strong latent heat losses and vertical oceanic convective mixing, resulting in an intense wintertime SST cooling in the northern Arabian Sea (Figure 2d) [*de Boyer Montégut et al*., 2007]. A cooling of weaker amplitude, due to similar mechanisms, also occurs in the northern Bay of Bengal. As a result of the northern IO cooling and of maximum solar insolation south of the equator, surface temperature maxima are located between the equator and 10°S and are tilted in a southwest-northeast direction, expanding from the Mozambican to the Java coasts (Figure 2d). Maximum precipitations display a similar southwest-northeast orientation but are located 5°S of the maximum SST. Precipitation extends northward as far as Sri Lanka, with very weak precipitations north of 10°N.

Both experiments reproduce qualitatively these observed wintertime features, with pattern correlations ranging from ~0.95 for SST (Figures 2e and 2f) to ~0.7 for sea level (Figures 2b and 2c). A detailed examination however reveals systematic biases. First, the negative sea level anomaly in the eastern equatorial IO and eastern and northern rim of the Bay of Bengal is overestimated, presumably because of too strong

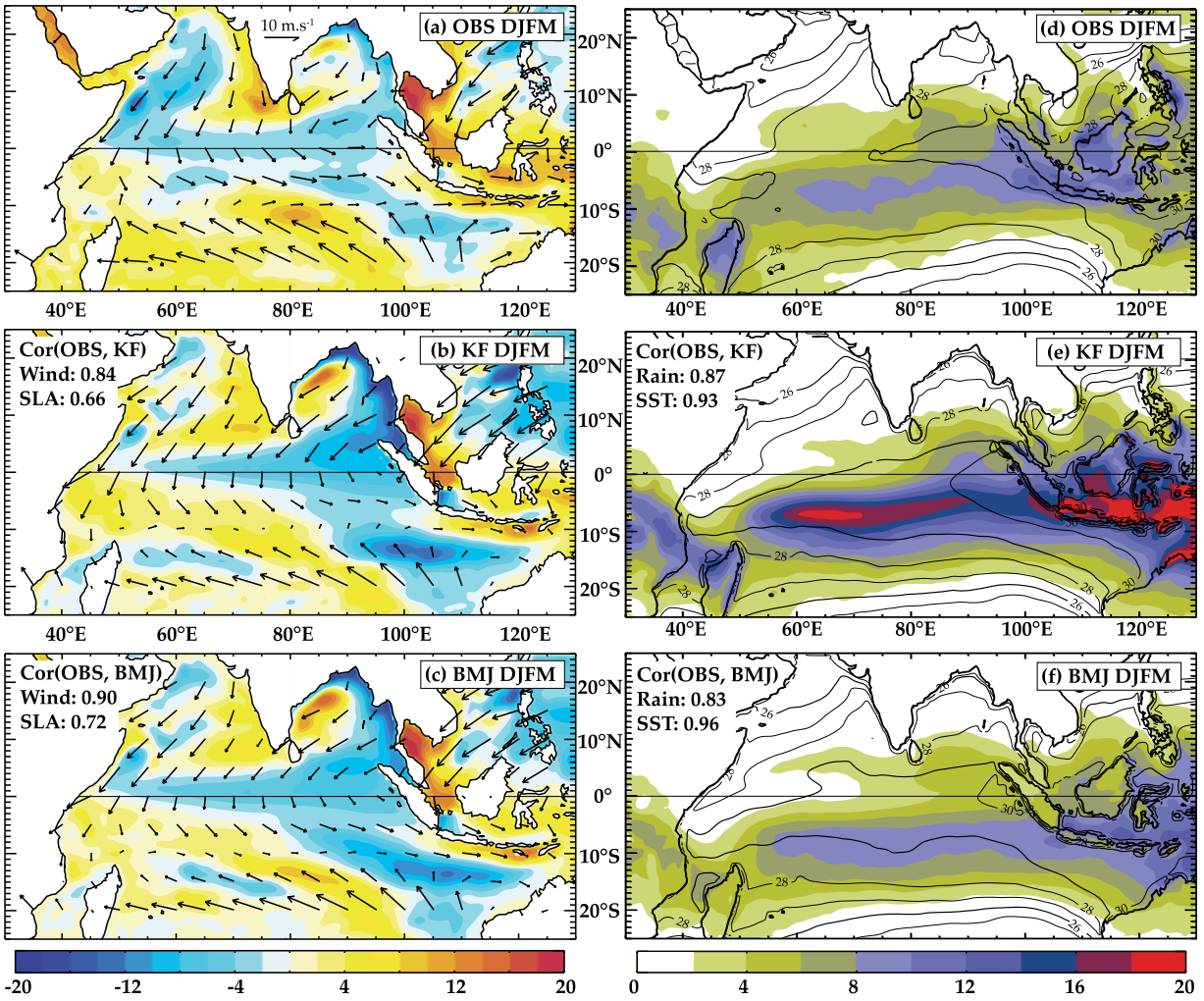

Figure 2. Winter (DJFM) climatology of (left) sea level anomalies (color, in cm) and 10 m wind (vector) and (right) rainfall (color, in mm d^{-1}) and SST (contour, in °C) for (top) observations, (middle) KF, and (bottom) BMJ experiments. The pattern correlations with observations are also given in the middle and bottom plots.

westerlies along the equator in boreal fall. The KF simulation is slightly too warm and strongly overestimates the amount of rainfall which maximum is located over the warmest waters (Figure 2e). Maximum precipitation in BMJ experiment is located 5°S of maximum SST as in observations but the tropical convergence zone orientation is too zonal (Figure 2f).

Figure 3 shows the 10 m wind, sea level, SST, and precipitation boreal summer (June–September) climatology from the observations and the two experiments and illustrates key aspects of the summer monsoon. The intense solar heating over the northern hemisphere during late spring and early summer favors the development of a heat low over the Asian continent. The resulting land-sea thermal and pressure contrast generates cross-equatorial low-level winds over the western IO/east African highland (Figure 3a) and a westerly flow extending from the Arabian Sea to the South China Sea resulting in a strong moisture flux toward the Asian landmass, initiating precipitation there (Figure 3d). The orographic structure of the Asian landmass provides anchor points where the maximum monsoon rainfalls are concentrated, especially along the Western Ghats, the Burmese coast, and the Philippines (Figure 3d). During this season, maximum SST are observed in the equatorial region and in the northern part of the Bay, while the western Arabian Sea is characterized by a very strong cooling as a result of coastal upwelling along the coast of Oman and Somalia in response to the strong southwesterly winds of the Findlater jet (Figure 3d), which prevents atmospheric convection to occur in the western part of the basin. Sea level patterns are usually opposite to those found

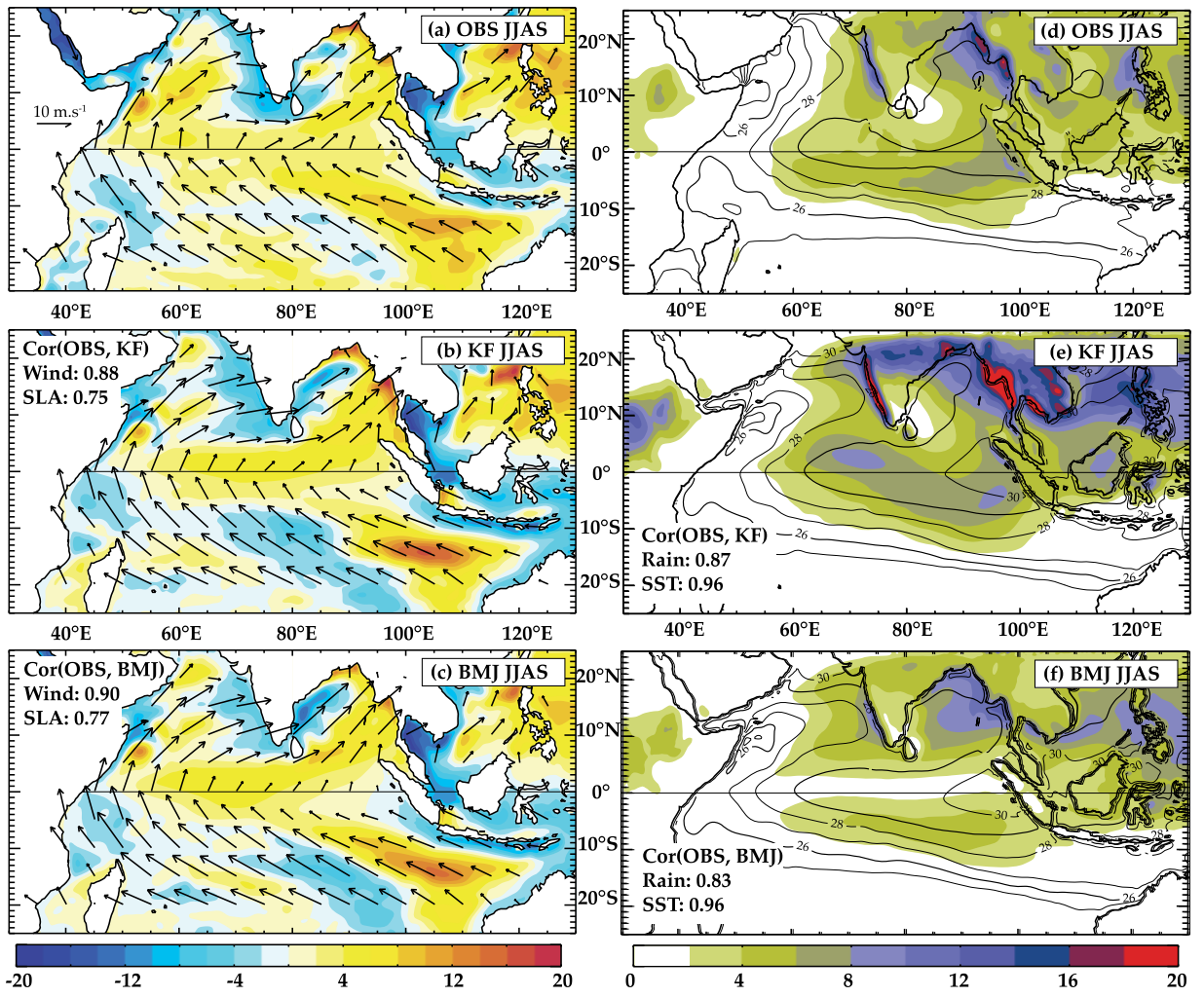

Figure 3. Summer (JJAS) climatology of (left) sea level anomalies (color, in cm) and 10 m wind (vector) and (right) rainfall (color, in mm d^{-1}) and SST (contour, in °C) for (top) observations, (middle) KF, and (bottom) BMJ experiments. The pattern correlations with observations are also given in the middle and bottom plots.

during the winter season (Figure 3a). In particular, alongshore winds, which develop off Java and Sumatra, result in a coastal downwelling signal there and sea level rise offshore.

Both simulations generally reproduce these features, with correlation patterns ranging from ∼0.75 for sea level (Figures 3b and 3c) to ∼0.95 for SST (Figures 3e and 3f). The largest SST bias for both experiments occurs in the Oman upwelling, whose intensity is locally underestimated by a large amount (∼4°C). While the monsoon over the Bay of Bengal is too zonal in most CMIP models [*Sperber et al.*, 2012], its orientation is properly represented in our experiments (Figures 3b and 3c). The precipitation patterns in BMJ and KF are also accurately captured, with correlation patterns of 0.83 and 0.87, respectively. The relatively high horizontal resolution of the atmospheric component allows properly capturing the main orographic features of the Asian landmass and the associated precipitation maxima (Figures 3e and 3f). The modeled precipitation patterns over the Indian subcontinent are also realistically captured, with a maximum of precipitation over the foothills of the Himalayas and a minimum of precipitation over southeastern India and Sri Lanka. As for winter, the KF simulation overestimates rainfall by ∼50–100% over the northern part of the domain (Figure 3e). In contrast, the BMJ simulation slightly underestimates rainfall amount south of 5°N, this bias being most pronounced in the central and eastern equatorial IO (Figure 3f).

The ability of the simulations to capture the annual cycle of the Indian summer monsoon, including the northward propagation of the continental rainfall band, is further evaluated in Figure 4 that displays a

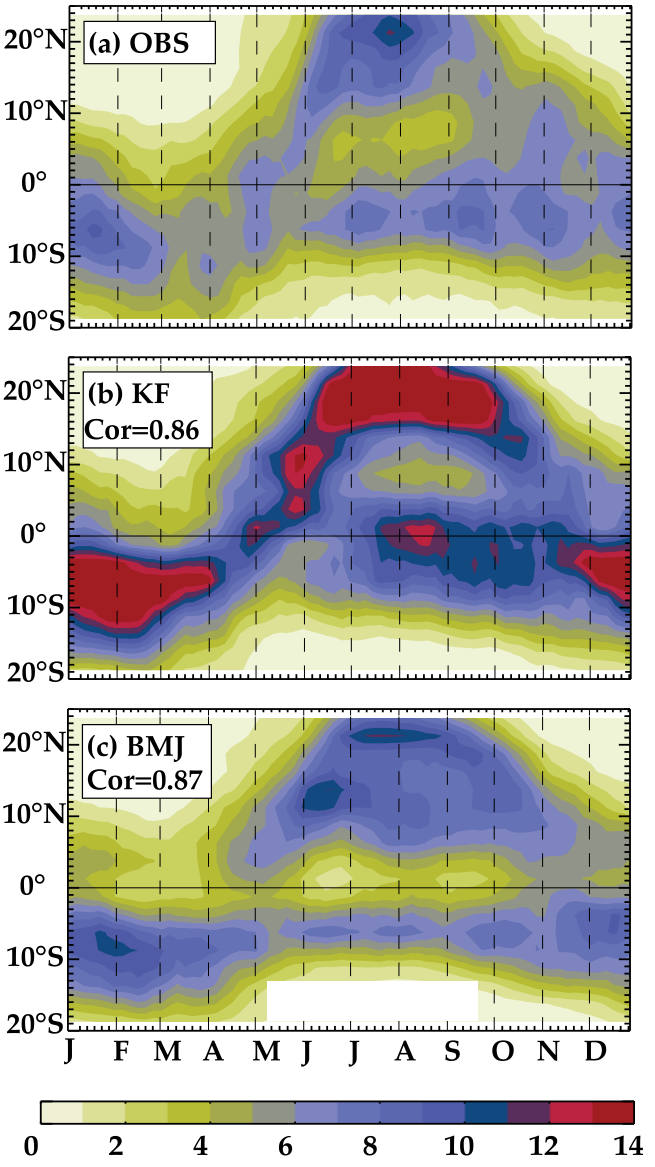

Figure 4. Seasonal evolution of averaged rainfall (in mm d^{-1}) between 70°E and 90°E from (a) observations, (b) KF, and (c) BMJ experiments. The pattern correlations with observations are also given in the middle and bottom plots.

latitude-time diagram of rainfall averaged between 70°E and 90°E. From May onward, observations indicate the formation of two rainfall maxima (Figure 4a), with oceanic rainfall near 5°S that reach a maximum in January and a northern rainfall band associated with the Indian monsoon. The northward shift of precipitation in May corresponds to the monsoon onset, which results in intense rainfall (larger than 6 mm/d) over the southern tip of India (~10°S) from early June onward. Continental rainfalls then reach their maximum amplitude in late July at about 20°N. After this date, the northern rainfall band shifts back southward to merge with the southern band around November.

Both KF and BMJ simulations represent very accurately the monsoon evolution, with a pattern correlation exceeding 0.85 (Figures 4b and 4c), while the best CMIP models are below 0.8 for the same metric [*Sperber et al.*, 2012]. The maximum precipitation over north India occurs in July and the northern precipitation band merges back with the southern one in November for both simulations. The KF simulation however displays the largest biases, with too intense rainfall throughout the year, and an earlier than observed monsoon onset. In the BMJ simulation, the continental monsoon precipitation maximum extends too far south.

4. Intraseasonal Variability

There is a very clear intraseasonal variability in the IO, at several time scales (10–20 and 30–90 days time scales), and different seasons (south of the equator in boreal winter, and in the NIO in boreal summer). Here we will concentrate on the northward propagating active/break phase of the summer monsoon [e.g., *Goswami*, 2005].

Figure 5 provides a validation of the amplitude of intraseasonal (30–90 days) variability of precipitation for the summer season. Observed summer intraseasonal rainfall variability displays three clear maxima in the IO, located along the western coast of India, just south of the equator around 90°E and in the north-eastern part of the Bay of Bengal (Figure 5a). Both simulations reproduce the location of these maxima, with KF overestimating their amplitude (Figure 5c) while the BMJ simulation underestimates it, in particular over land.

A simple index of active and break monsoon phases can be constructed by taking the difference between Bay of Bengal (70°E–95°E, 10°N–20°N) and equatorial IO (70°E–95°E, 5°S–5°N) 30–90 day filtered

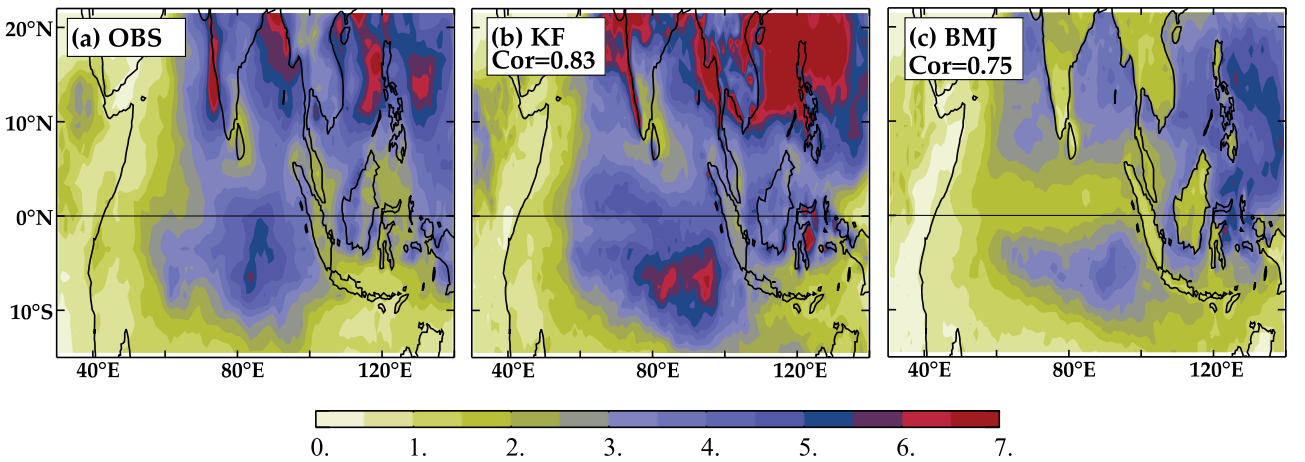

Figure 5. Standard deviation of rainfall (in mm d^{-1}) intraseasonal (30–90 days) variability in boreal summer for (left) observations, (middle) BMJ, and (right) KF experiments. The pattern correlations with observations are also given in the middle and right plots.

precipitation [e.g., *Goswami*, 2005]. Figure 6 displays lag regressions of the summer intraseasonal precipitation and surface wind signals onto this normalized index, hence illustrating the typical time evolution of summertime intraseasonal variability. The observed pattern at lag −20 is characteristic of a break phase, with decreased wind over the northern IO and the monsoon jet deflected around the southern tip of India [e.g., *Joseph and Sijikumar*, 2004]. This phase is characterized by increased precipitation south of the equator extending eastward to the Maritime Continent while a tilted band of suppressed precipitation occupies the

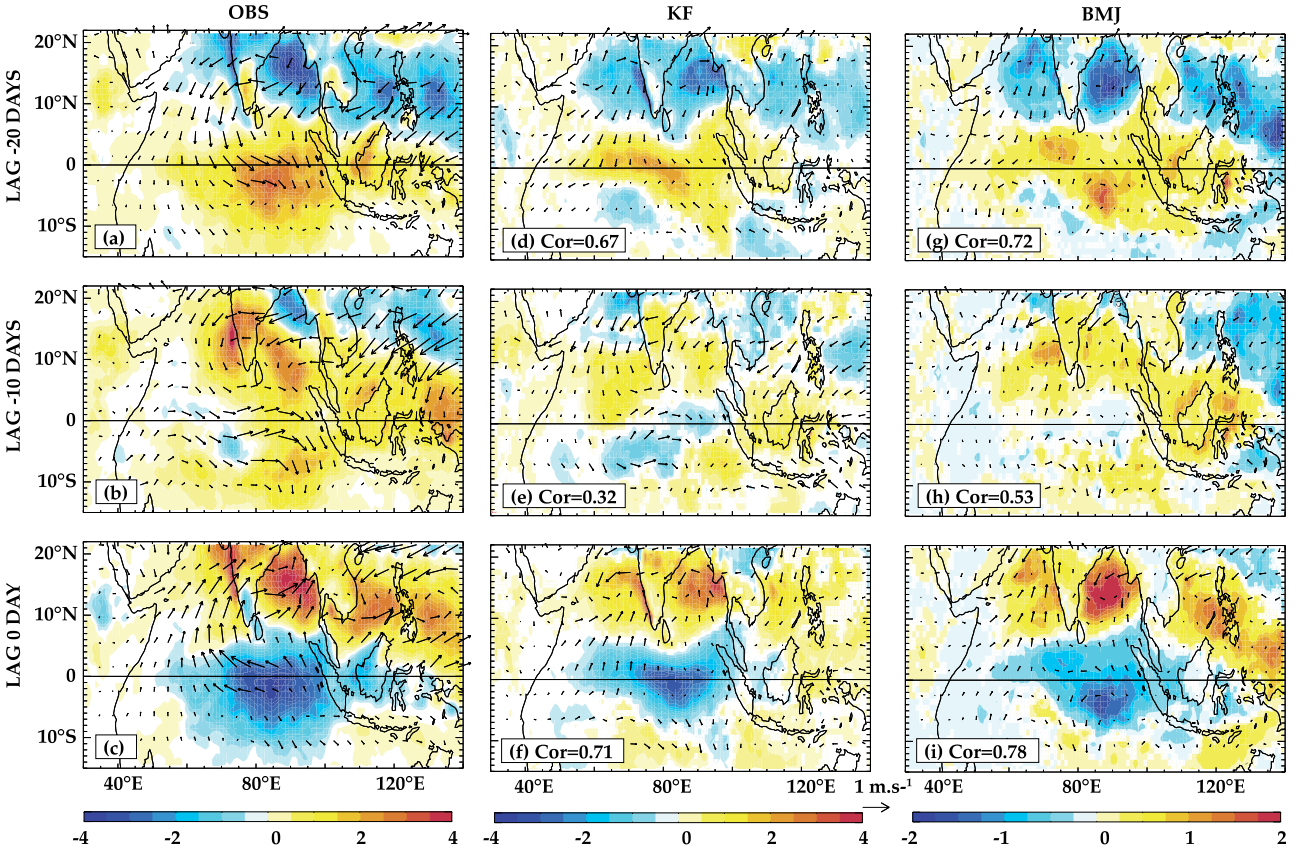

Figure 6. Lag correlation of summer monsoon index with intraseasonal (30–90 days) precipitation (color, in mm d^{-1}) and wind (vector) for (left column) observations, (middle column) KF, and (right column) BMJ experiments. The lag correlations are displayed for a lag (top) −20 days, (middle) −10 days, and (bottom) 0 days. The pattern correlations with observations are also given in the middle and right plots. The BMJ simulation has weak rainfall and uses a different color bar from the two other simulations.

Northern IO, extending from the Arabian Sea and the Indian subcontinent to the Western Pacific (Figure 6a). The tilted band of excess precipitation progresses northward during the transition phase (lag −10, Figure 6b), with maximum rainfall anomalies over the southern part of the Bay and southern India. Finally, the pattern at lag 0 displays an active phase with an increased monsoon flow and precipitation across the Indian subcontinent and northern part of the Bay (Figure 6c).

Both simulations are able to simulate the main characteristics of the active and break precipitation patterns. The BMJ simulation however behaves best in terms of precipitation patterns with highest correlation patterns (ranging from 0.53 for the transition phase to 0.78 for the active phase). This simulation is able to reproduce the northward propagating precipitation anomalies and their associated northwest to southeast tilt (Figures 6g–6i). The main caveat of BMJ active/break phases is that the precipitation signal is two to three time weaker than observed amplitudes (notice the different scale used for BMJ simulation), this bias being emphasized over land. In contrast, the KF simulation largely fails to reproduce the observed tilt of the rain band (Figures 6d–6f) and poorly reproduces the phase transition with a correlation pattern of 0.32, suggesting a standing oscillation rather than a northward propagation (Figure 6e). While the two simulations display some skill in reproducing the intraseasonal precipitation patterns, it is less obvious for the wind patterns. Both models have a stronger/weaker low-level monsoon jet during the active/break monsoon phase although not as clearly as observations, and they do not reproduce the monsoon jet deflection around the southern tip of India and wind signals over the Bay of Bengal.

5. Interannual Variability

The JJAS Indian Summer Monsoon Rainfall (ISMR) index is defined as the area weighted mean rainfall over India, based on the observational data set produced by the Indian Institute of Tropical Meteorology (IITM). Figure 7a displays time series of the interannual evolution of the ISMR for the two simulations and observations. Both model and observations display weakly negative correlation between the Indian monsoon and ENSO over 1990–2009 (Figure 7a), suggesting that the ISMR and ENSO are relatively independent over the recent period, as observed by *Krishna Kumar et al.* [1999] over recent decades.

The IOD has a strong influence on the climate of the Indian sector at interannual time scales [e.g., *Yamagata et al.*, 2004]. In observations, positive IOD events are characterized by a cooling along the coast of Java and Sumatra (Figure 8d) and anomalous easterly winds in the central IO (Figure 8a), with the two anomalies

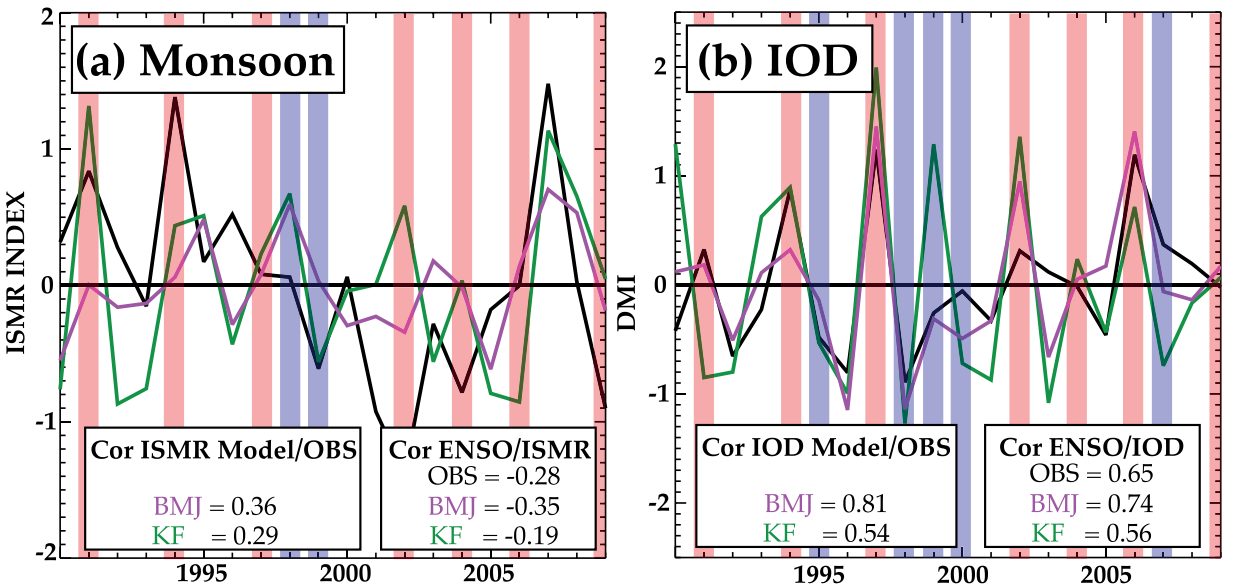

Figure 7. Interannual variability of the (a) Indian Summer Monsoon Rainfall (ISMR) in JJAS (in mm d^{-1}) and (b) Dipole Mode Index (DMI) in SON (in °C) for observations (black), KF (green), and BMJ (pink) experiments. The correlations of modeled with observed ISMR, modeled and observed ISMR time series with Niño34 SST in JJAS (summer ENSO index) are displayed in Figure 7a. Similarly, correlations of modeled with observed IOD time series and modeled and observed IOD time series with Niño34 SST in NDJ (winter ENSO index) are displayed in Figure 7b. The vertical stripes indicate El Niño years (red) and La Niña (blue) occurrences for (a) summer and (b) winter.

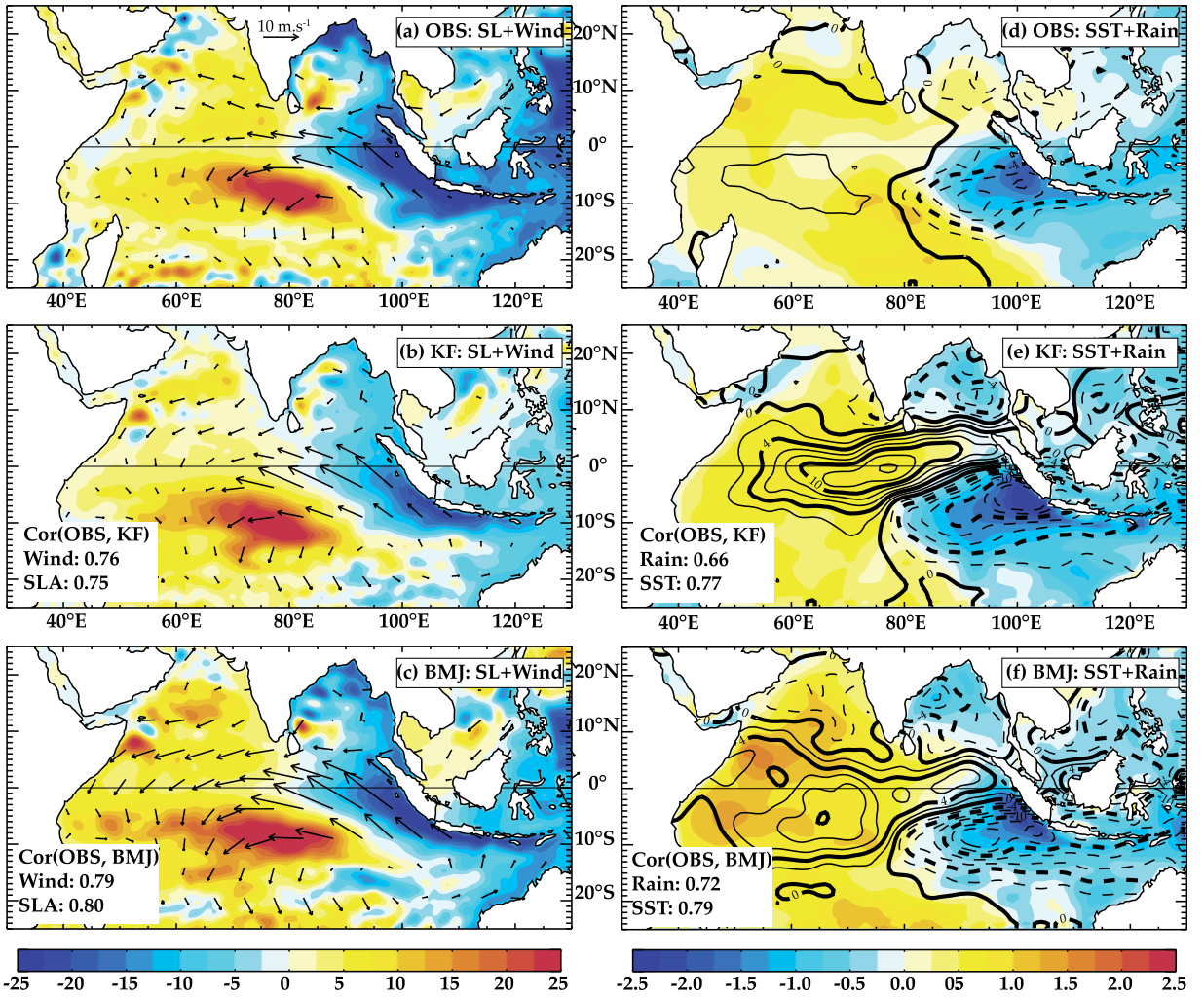

Figure 8. Composite of the half-difference between positive IOD and negative IOD in fall (SON) in (left) SLA (color, cm) and 10 m wind (vectors, in m s^{-1}) and (right) SST (color, in °C) and rainfall (contour, mm d^{-1}) for (top) observations, (middle) KF, and (bottom) BMJ experiments. The pattern correlations with observations are also given in the middle and bottom plots.

enhancing each other through a positive feedback loop. The eastern IO cooling also locally drives a strong decrease in precipitation while the western IO warming coincides with a slight rainfall increase (Figure 8d). The anomalous equatorial easterly winds force eastward-propagating Kelvin waves, which raise the thermocline along the Sumatra coast and in the Bay of Bengal (Figure 8a). The IOD-related wind pattern also induces Ekman-driven convergence south of the equator that results in a deepening of the thermocline between 5°S and 12°S in the central IO, which then propagates westward as a Rossby wave [e.g., *Webster et al.*, 1999]. This thermocline deepening contributes to SST warming in this region [e.g., *Xie et al.*, 2002] (Figure 8d).

Both simulations reproduce reasonably well the SST, wind, and sea level perturbations associated with IOD events, with correlation patterns with observations generally exceeding 0.75. However, the BMJ simulation slightly overestimates the amplitude of the wind anomalies all over the western equatorial IO (Figure 8c). The largest model bias is associated with rainfall, with a large overestimation of the precipitation increase over the western IO in both simulations (Figures 8e and 8f).

Figure 7b displays the observed and simulated Dipole Mode Index (DMI) [*Saji et al.*, 1999] time series. Interestingly, both simulations are to a certain extent phased with observed IOD variability, being able to simulate positive IOD events in 1994, 1997, and 2006 and negative IOD events in 1992, 1996, and 1998, as in observations. This phasing is particularly striking for the BMJ simulation, which displays a 0.81 correlation

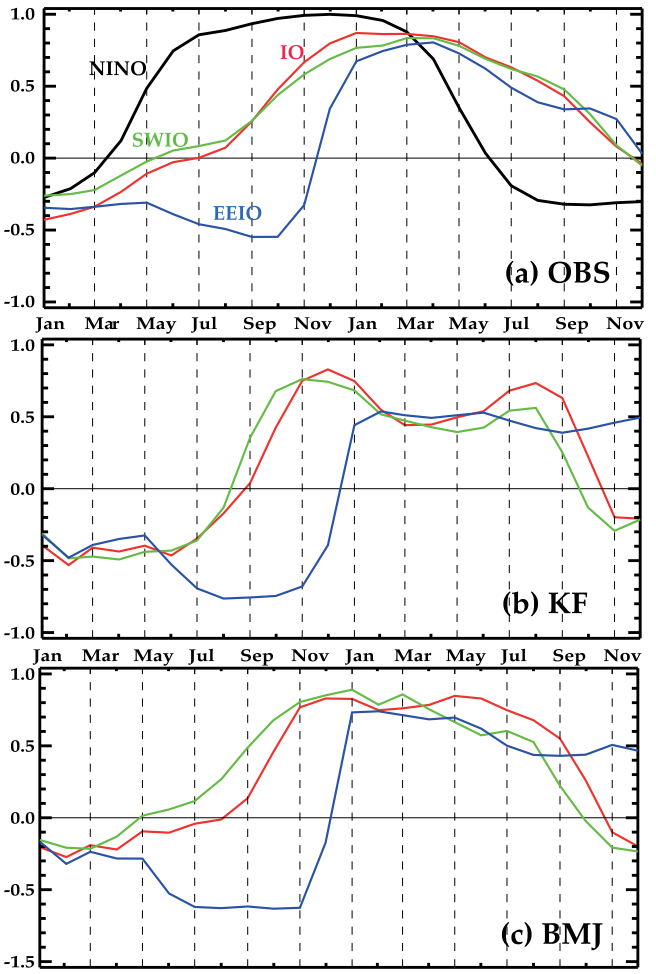

Figure 9. Lag correlation of monthly SST averaged over the tropical IO (40–100°E, 20°S–20°N; red), the southwest IO (50–70°E, 15–5°S; green), and the eastern equatorial IO (90–110°E, 10°S–0°; blue) with Niño3 (90°W–150°W, 5°N–5°S) SST index for (a) observations (similar to the analysis in *Schott et al.* [2009]), (b) KF, and (c) BMJ simulations.

with the observed DMI time series. The KF simulation exhibits a more biennial tendency, with a strong positive IOD event simulated in 1999 that is neither present in observations nor in the BMJ simulation. While the IOD is an intrinsic mode of variability of the ocean-atmosphere system in the IO sector, there is a tendency of IOD events to co-occur with ENSO [e.g., *Yamagata et al.*, 2004]. *Annamalai et al.* [2003] suggest that El Niño events tend to produce easterly anomalies over the IO in spring, which can trigger a positive IOD event. In our model, the effect of ENSO is transmitted through the imposed lateral boundary conditions. The agreement between observed and modeled DMI time series seems to confirm the influence of ENSO on the triggering of the IOD in our model.

The influence of ENSO on IO interannual SST variations is further illustrated in Figure 9 (first plot of which is inspired from a similar analysis shown in *Xie et al.* [2009] and *Schott et al.* [2009]). In observations, the tropical IO gradually warms during an El Niño event, starting in summer preceding El Niño peak and persisting several months after the El Niño demise [e.g., *Xie et al.*, 2009] (Figure 9a). The western IO SST displays a similar evolution to the tropical IO. In contrast, the SST evolution is different in the eastern equatorial IO. This region cools during the developing phase of El Niño in response to intensified southeasterlies off Java and Sumatra associated with an anomalous high-pressure system part of ENSO, favoring the development of an IOD event. From November, the southeasterlies weaken and the SST anomalies there switch abruptly from negative to positive.

Both BMJ and KF experiments accurately capture the IO SST evolution in response to ENSO forcing, including the prolonged IO warming (Figures 9b and 9c). It is therefore likely that the ENSO signal, particularly strong over the eastern boundary of the domain, is accurately transmitted in the IO domain.

6. TC Activity

Figures 10–12 describe the observed and simulated TC spatial distribution and seasonal cycle in the IO. Figure 10 shows TC genesis and tracks density spatial distribution, while Figure 11 displays the seasonal cycle of cyclogenesis in the southern and northern IO. Figure 12 exhibits the modeled and observed seasonal evolution of Genesis Potential Index (GPI) [*Emanuel and Nolan*, 2004] along with each of its dynamical and thermodynamical components, in order to validate the model ability to reproduce the main large-scale environmental parameters responsible for the TCs distribution.

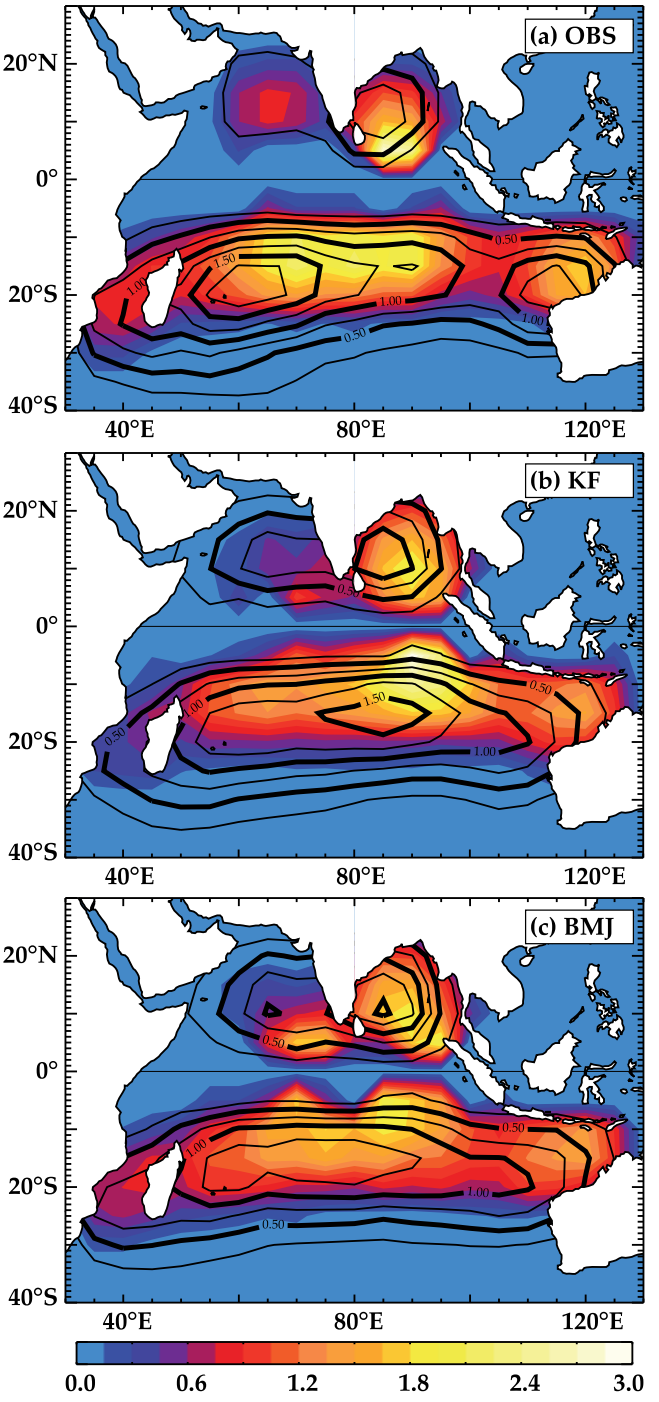

Figure 10. Spatial distribution of cyclogenesis (color, in % of the total number of formed cyclones per 5° × 5° bins) and TC density (contour, in % per 5° × 5° bins) for (a) observations, (b) KF, and (c) BMJ experiments.

TCs formation and occurrence regions appear to be relatively well captured by the two simulations (Figure 10). Let us first discuss the southern part of the basin. Observed tropical cyclogenesis occurs mostly between 5°S and 25°S. The KF and BMJ simulations capture this feature reasonably well, although with a slight equatorward shift of the maximum cyclogenesis. Simulated TCs density tracks also agree reasonably with observations with a poleward-shifted distribution relative to cyclogenesis (TCs mostly occur between 10°S and 30°S). The maximum TCs density is however shifted eastward in KF simulation and none of the simulations reproduce the gap in track density around 100°E, east of the West Australian coast. Observed and modeled TCs usually travel southwestward between 10°S to 15°S to then deviate and travel in a southeastward direction between 20°S and 30°S, being advected by climatological tropospheric winds (not shown). The seasonal distribution of cyclogenesis (Figure 11a) and TCs density (not shown) is also well captured by the simulations with the largest number of storms developing during the local summer season, i.e., between December and March, in the southern IO. While both simulations reasonably reproduce the seasonal evolution of TCs genesis and occurrence, KF however produces twice as much TCs as observations (Figure 11a). In contrast, the BMJ experiment does simulate a realistic number of storms. This seasonal cycle is well captured by the Genesis Potential Index in both simulations (Figures 12a–12e). High midtropospheric relative humidity, low vertical shear, and high maximum potential intensity combine to favor most cyclogenesis in the southern IO during austral summer [*Menkes et al.*, 2011]. Although the seasonal evolution of each of the GPI components is well captured by both simulations, the analysis of the individual terms reveals that mean modeled vorticity at 850 hPa and vertical wind shear are overestimated. The GPI is not able to capture the differences in terms of genesis number

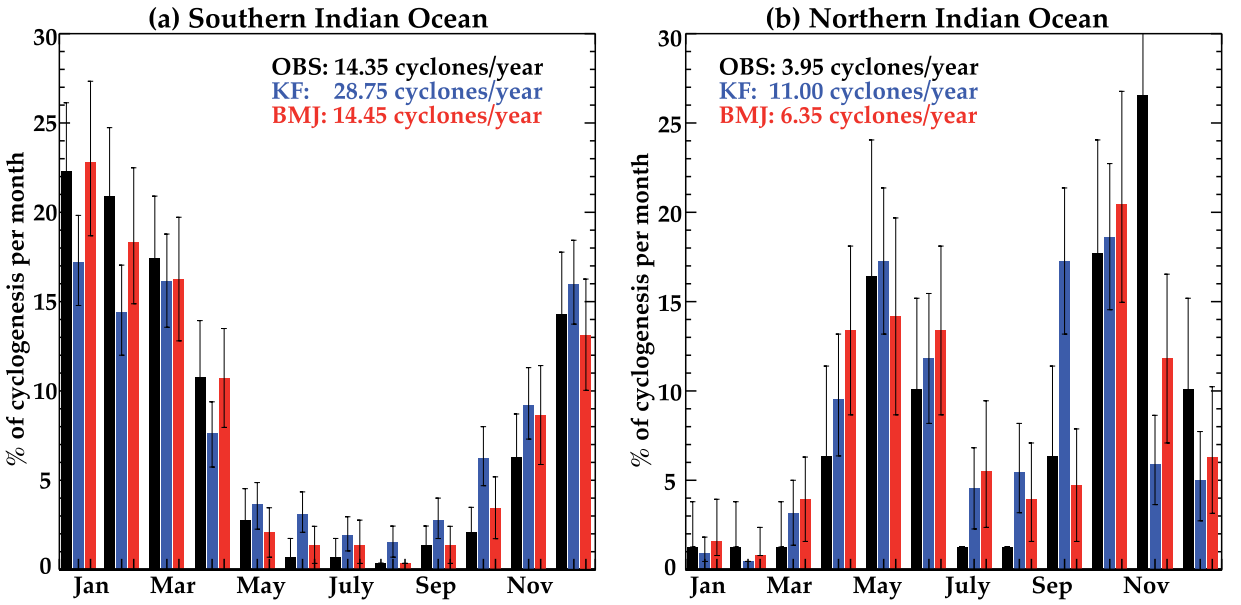

Figure 11. Seasonal cycle of relative cyclogenesis (in % of the total number of cyclones per month) for observations (black), KF (blue), and BMJ (red) experiments for (left) the southern and (right) northern Indian Ocean. The whiskers display 95% confidence interval on monthly cyclogenesis values based on a Student's *t* test.

observed between KF and BMJ experiments. This suggests that the large-scale environment may not be responsible for the different number of TCs generated in each simulation. The convective parameterization hence probably acts locally by directly influencing the cyclogenesis process rather than by modifying the large-scale environment favorable to cyclogenesis. This issue will be further addressed in the discussion section.

In the northern IO, both observations and simulations show a maximum cyclogenesis and TC density in the central part of the Bay of Bengal centered around 10°N (Figure 10). In this basin, most observed and modeled TCs travel northward and/or westward (not shown). While weakening over the Indian peninsula, some storms are able to reintensify when reaching the Arabian Sea to further pursue their trajectory westward. Less frequent tropical storm formation occurs in the Arabian Sea, with three times less TCs as compared to the Bay of Bengal for observations and simulations. As in the southern hemisphere, maximum modeled cyclogenesis in the Arabian Sea is however located equatorward as compared to observations (5°N against 12°N). The northern IO is known to exhibit a very peculiar bimodal seasonal distribution of tropical cyclogenesis (Figure 11b): they indeed preferentially occur during the pre (April–June) and postmonsoon (September–December) seasons, with much fewer TCs in June–July and almost no TCs in the early part of the calendar year. This bimodal distribution can be attributed to the very strong increase in vertical wind shear along with a strong decrease in maximum potential intensity during summer monsoon (Figures 12f–12j), preventing the formation of tropical storms during that season in agreement with previous studies [*Tippett et al.*, 2011; *Menkes et al.*, 2011]. The KF and BMJ simulations accurately capture this specific bimodal cyclogenesis distribution (Figure 11b), along with their large-scale atmospheric drivers (Figures 12f–12j). As for the southern IO, the largest bias is an overestimation of the number of TCs in both simulations (by 60% in BMJ and 180% in KF).

The intensity distribution of simulated and observed TCs for both hemispheres is summarized by histograms of the TCs wind and sea level pressure distribution (Figure 13). In observations, surface wind speed can reach 70 m s^{-1} for strongest TCs in both the Bay of Bengal and Southern IO, with minimum central pressure down to ~915 hPa (category 5 on the Saffir-Simpson scale). For both hemispheres, the KF experiment is able to simulate TCs classified as intense tropical cyclones (>46 m s^{-1}) but they however never exceed category 3. The most intense cyclone produced by the KF experiment developed in the Northwest Australian basin, reaching a surface maximum wind speed of ~56 m s^{-1} and an associated central pressure of about 928 hPa. In contrast, BMJ experiment simulates much weaker TCs, never experiencing TCs stronger than category 2. The most intense cyclone simulated by BMJ experiment also occurred in the southern IO

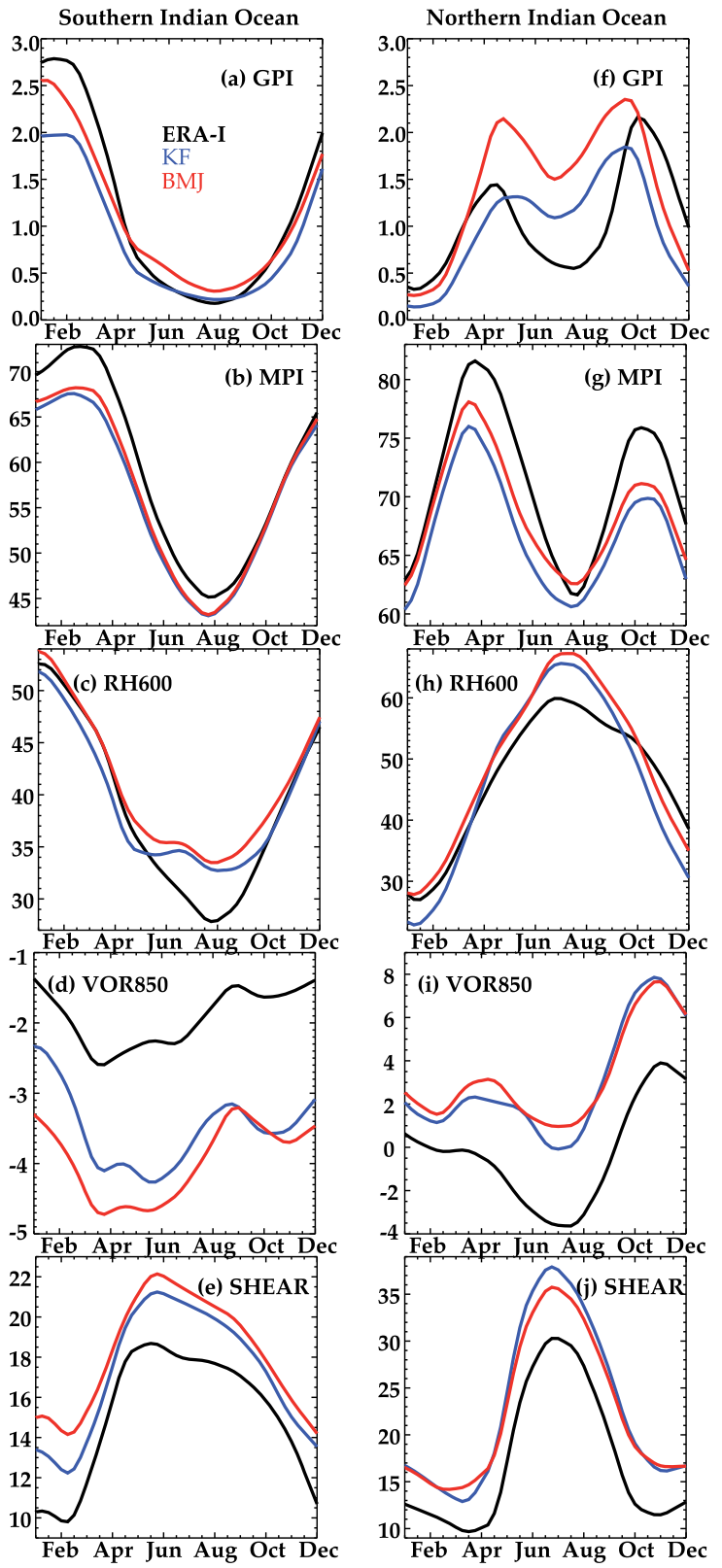

Figure 12. Seasonal evolution of (a) Genesis Potential Index (GPI), (b) Maximum potential intensity (MPI), (c) relative humidity at 600 hPa, (d) vorticity at 850 hPa, and (e) vertical wind shear in the Southern Indian Ocean for observations (black), KF (blue), and BMJ (red) experiments. (f–j) Same but for the Northern Indian Ocean.

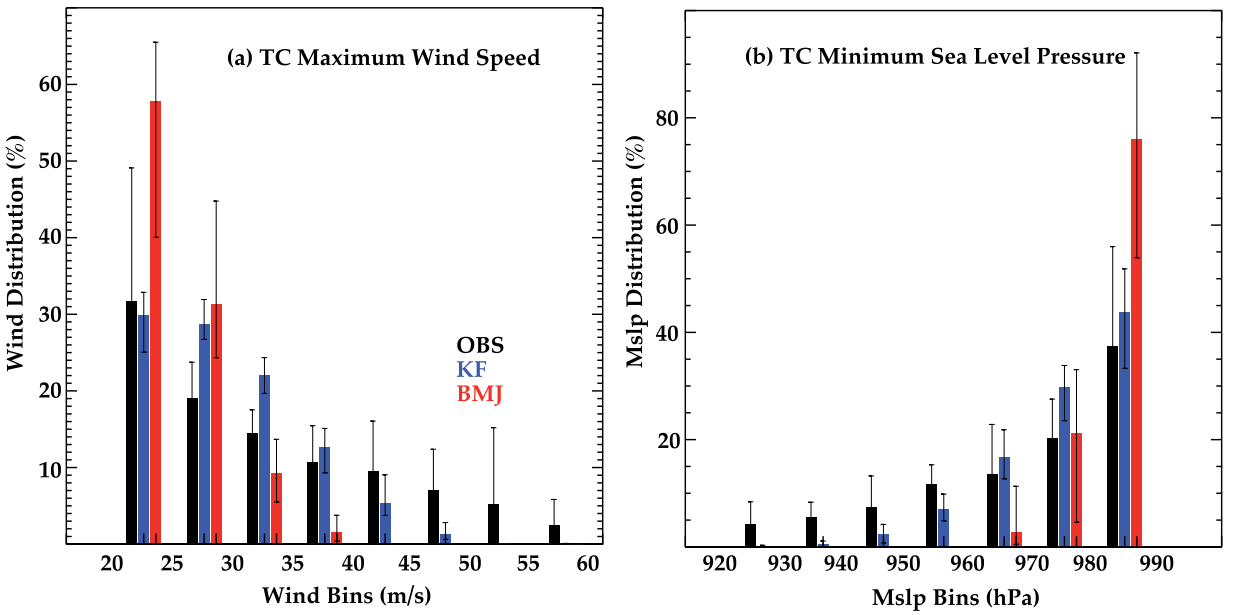

Figure 13. (left) Maximum wind intensity and (right) minimum sea level pressure distribution in observations (black), KF (red), and BMJ (blue) simulations for all Indian Ocean TCs.

but in the Mozambique Channel, reaching a surface maximum wind speed of ~40 m s^{-1} and central pressure of about 970 hPa. Although the KF experiment simulates stronger TCs than BMJ, both simulations fail to reproduce the strongest TCs.

Indeed, the 25 km model resolution does not allow to fully capture the sharp eyewall structure of the tangential winds and underestimates the strongest eyewall updrafts which contributes to the warming of the core region [*Gentry and Lackmann*, 2010]. A composite of the modeled radial wind and precipitation profile is provided in Figure 14. This composite is compared with idealized radial structures for wind and rainfall, respectively, from the *Willoughby et al.* [2006] and *Tuleya et al.* [2007] formulations (discussed in section 2).

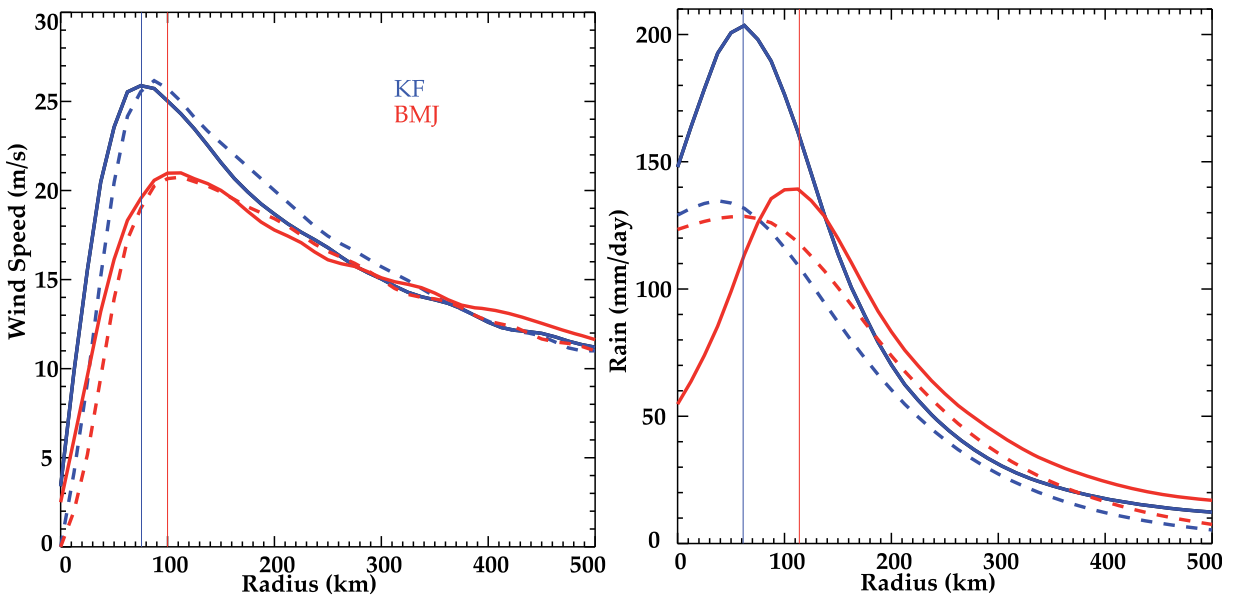

Figure 14. (a) Composite of TCs radial wind profile as a function of the distance to the TC center directly derived from the model (plain) and reconstructed using *Willoughby et al.* [2006] formulation (dashed) for KF (blue) and BMJ (red) simulations. (b) Composite of TCs rainfall profile directly derived from the model (plain) and reconstructed using *Tuleya et al.* [2007] formulation (dashed) for KF (blue) and BMJ (red) simulations. Vertical lines indicate the wind speed and precipitation maxima for both simulations.

The KF experiment generally simulates a smaller, more realistic radius of maximum wind speed (~75 km) compared to the BMJ experiment (~100 km). These two radius are however larger than the mean observed value of 50 km, but expected from such 1/4° resolution simulations [*Gentry and Lackmann*, 2010].

The reconstructed wind profiles using the *Willoughby et al*. [2006] analytical formulation agrees well the actual simulated profile for both KF and BMJ. This suggests that, for a given storm intensity, these experiments are able to simulate a realistic spatial distribution of wind. Since weak storms do exhibit larger radius of maximum wind than stronger storms, the overestimated radius of maximum wind (especially in BMJ) is therefore likely to result from the absence of the strongest (and smallest) TCs in the model simulations. The precipitation profile also displays a smaller radius of maximum precipitation for the KF experiment (~60 km), compared to BMJ (~110 km). The composite rainfall radial profiles reconstructed from the simulated TCs intensity and *Tuleya et al*. [2007] formulation are also shown in Figure 14b. They illustrate that the KF simulation has a reasonable radius of maximum precipitation, but strongly overestimates rainfall in the TC core. On the other hand, BMJ produces a more reasonable amount of rainfall near the eyewall, but produces maximum rainfall at an almost twice too large radius. Both simulations also tend to produce a dry region at the center of the storm, which is almost absent from the *Tuleya et al*. [2007] formulation. The fact that the KF scheme produces larger than observed precipitations for a given wind intensity also suggests that the KF scheme is too active in tropical cyclones which leads to the greater TC intensity when compared to the BMJ scheme as observed in Figure 13.

7. Summary and Discussion

7.1. Summary

In this paper, we describe and validate the newly developed NOW ocean-atmosphere regional model that couples the NEMO ocean model with the WRF atmospheric model through the OASIS3 coupler. Here this regional coupled model is applied to the Indian Ocean sector, with a common 1/4° horizontal grid for the oceanic and atmospheric components. Two long-term experiments were performed over the 1989–2009 period, using either the Betts-Miller-Janjic (BMJ) or Kain-Fritsch (KF) cumulus parameterizations. This allows us both to validate the main features of the simulated climate (seasonal cycle, intraseasonal variability, interannual variability, TC structure, and distribution) in this new model, and to assess the sensitivity of the model results to the cumulus parameterization. To our knowledge, it is the first attempt to run such long-term simulations to investigate the ability of a regional coupled model to simulate the climatology of TC statistics in the IO.

The two experiments generally reproduce the IO seasonal cycle accurately. The model captures the spatial structure of the monsoon wind reversal and associated thermocline-depth variations accurately, along with the northward migration of warmest SST and rainfall during boreal summer. In particular, the relatively high horizontal resolution of the atmospheric component allows properly capturing the main orographic features of the Asian landmass, resulting in a realistic monsoon jet orientation and realistic location of the simulated precipitation maxima along the Western Ghats, the foothills of the Himalaya, and the Burmese coast. At intraseasonal time scales, the model shows reasonable skill in simulating the main characteristics of the active and break phases, although with underestimated precipitation and surface wind signals.

At interannual time scales, the IO climate is modulated by the internally generated IOD and the remote influence of ENSO. As in observations, the modeled IO SST gradually warms during an El Niño event, starting in the summer preceding El Niño peak and persisting several months after the El Niño demise. During positive IODs, the model displays realistic easterly wind anomalies in the central IO, and captures the spatial structure, timing, and amplitude of the associated anomalous cooling and thermocline shoaling along the coasts of Java and Sumatra. However, the model strongly overestimates the amplitude of the precipitation increase in the western IO. Interestingly, the timing of IOD occurrences in the model matches observed events well, and both model and observed IOD indices are significantly correlated with ENSO. These results seem to confirm previous studies [e.g., *Annamalai et al*., 2003] indicating that external ENSO forcing during spring (transmitted through the lateral boundary conditions in our model) can trigger an IOD event.

The relatively high resolution that is used here (0.25°) also allows simulating TCs, with realistic cyclogenesis and track density and a realistic seasonal cycle, including the observed bimodal distribution in the northern IO. The seasonal evolution of the large-scale atmospheric parameters involved in the TCs genesis is also

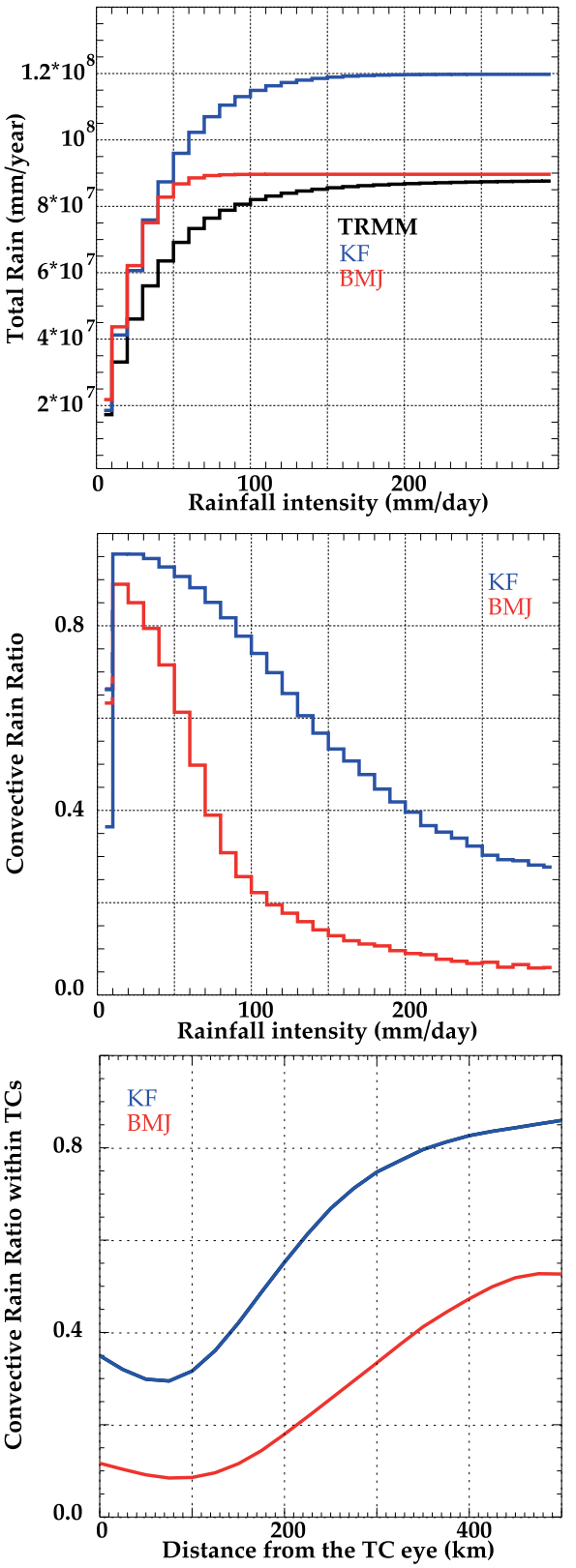

Figure 15. (a) Total integrated rainfall distribution (mm/yr) as a function of rainfall rates (mm/d) over the ocean for KF (blue) and BMJ (red). (b) Parameterized to total rainfall ratio (%) as a function of rainfall rates (mm/d). (c) Percentage of rainfall amount parameterized as a function of the distance to the composite TC center for KF (blue) and BMJ (red) simulations.

properly captured. The main discrepancy lies in the inability of the model to simulate the strongest TCs, with maximum model winds reaching $\sim$50 m s^{-1}, in contrast to $\sim$70 m s^{-1} in observations.

7.2. Sensitivity to Convective Parameterizations

Although the KF and BMJ simulations share a lot in common, there are noticeable differences in the atmospheric features simulated by these two experiments. The KF simulation usually produces much more rainfall than BMJ and observations, irrespective of the considered temporal and spatial scales. This is particularly true for the long-term mean, for which KF rainfall maxima are about twice larger than in BMJ experiment, which display more realistic (although slightly underestimated) rainfall amount.

Precipitation in atmospheric models is generally implicitly generated through convective parameterization schemes and explicitly through microphysics schemes. A reasonable simulation of the rainfall amount is particularly complex for mesoscale atmospheric models with resolution of the order of tens of kilometres, as it relies on a subtle balance between implicit and explicit cloud schemes that work concurrently. This balance is illustrated in Figure 15.

For low rain rates ($<$50 mm/d), both BMJ and KF overestimate the amount of precipitation by $\sim$30% over the ocean (Figure 15a). At those rain rates, parameterized rain accounts for most of the rainfall (80% for BMJ and 90% for KF, Figure 15b). The overestimated occurrence of weak rainfall rates hence largely results from an overly active convective scheme of both BMJ and KF, and not from explicitly resolved rainfall. The largest differences between KF and BMJ however appear at higher rain rates ($>$50 mm/d). In the observations, these rain rates account for 2.10^7 mm/yr, contributing to $\sim$25%

of the total rainfall amount (Figure 15a). While BMJ strongly underestimates the amount of precipitation at these rain rates ($\sim 7 \times 10^6$ mm/yr), KF overestimates this amount by 50% ($\sim 3 \times 10^7$ mm/yr). For BMJ, this underestimation can be attributed to a rapid decrease of the parameterized rain ratio for increasing rain rates, with a contribution of parameterized rainfall lower than 20% for rain rates greater than 100 mm/d (Figure 15b). The KF scheme remains very active even for the highest simulated rain rates ($\sim$250 mm/d) with an asymptotical minimal contribution of about 20–25%. BMJ is able to simulate a comparable total rainfall amount to the observed one (Figure 15a) despite a poorly simulated rainfall distribution: the rainfall overestimation at low rain rates compensates its underestimation at larger rain rates. The rain rate overestimation by the KF scheme, for rain rates up to 100 mm/d, results in an overestimation of the total rainfall. Similar conclusions are obtained for the same analysis over land (not shown).

Within TCs (Figure 15c), explicitly generated rainfall driven by intense vertical motions dominates inner core precipitation in both simulations. Within and near the eyewall, the convective scheme still produces 30% of the total rainfall amount for the KF parameterization while it is only 10% for BMJ. Further away from the TC core (500 km), most of the residual rainfall is parameterized in KF case ($\sim$85%), while the convective parameterization only accounts for $\sim$50% of total rainfall amount in the BMJ case. The smaller amount of rainfall generated by the parameterization hence results in a reasonable rainfall amount associated with the cyclone in BMJ (Figure 14b). On the other hand, the extrarainfall produced by the KF parameterization combines with the explicit rainfall to result in too much rainfall, especially near the eye (Figure 14b). The larger rainfall rates in the TC-eye in KF induce a stronger latent heating in the TC core, which leads to higher intensification rates and stronger TCs than in the BMJ simulation.

These results suggest that the KF cumulus parameterization may be overly active and/or too easily triggered by the environmental forcing when the atmospheric column is destabilized, especially at low rain rates. An overly reactive convective scheme could also result in a strong overestimation of the number of tropical convective disturbances, in line with the tendency of KF simulation to strongly overestimate the number of simulated TCs. The overestimation of the precipitation amount as simulated by the Kain-Fritsch cumulus parameterization has already been noticed for the South Atlantic Convergence Zone [*Gomes and Chou*, 2010]. It is therefore likely that the better performance of the KF experiment in simulating relatively intense TCs (as compared to BMJ) may also be a direct consequence of the KF scheme being overly reactive rather than a better designed convective parameterization.

A limitation of the discussion above is that each convective parameterization has tunable coefficients, some of which can lead to a very different behavior of the model [*Yang et al*., 2012]. The parameters used in the current paper correspond to the standard choices for the BMJ and KF parameterizations in the WRF model, but a different sensitivity may be obtained for a different tuning of those coefficients.

7.3. Perspectives

Although there is still room for improvement, the newly developed NOW regional ocean-atmosphere model reasonably simulates a wide range of phenomena, from small scale high-frequency atmospheric processes such as TCs, to large-scale climatic features such as the monsoon or the Indian Ocean Dipole. This model is therefore a versatile and relevant modeling tool to investigate the influence of air-sea interactions on the variability of the coupled system in the IO. Many previous studies did suggest that the negative feedback on TCs associated with air-sea interactions was strong and could not be neglected, but they generally did so by using relatively simple models [e.g., *Schade and Emanuel*, 1999] or in the framework of case studies [e.g., *Bender and Ginis*, 2000]. The two long simulations that we have performed provide a unique opportunity to study the influence of air-sea interactions on the tropical cyclone climatology, and we will do so in a future study.

Acknowledgments

The model described in this paper is available at IPSL (Institut Pierre Simon Laplace) website: http://forge.ipsl.jussieu.fr/now. Guillaume Samson was supported by the IS-ENES FP7-Project funded by the European Commission. The authors thank IFCPAR (Indo French Centre for Promotion of Advanced Research), New Delhi for funding of the proposal 4907-1, LEFE (Les Enveloppes Fluides et l'Environnement) program for funding of the proposal CYCLOCEAN AO2010–538863 and IDRIS for computing facilities.

References

Annamalai, H., R. Murtugudde, J. Potemra, S. Xie, P. Liu, and B. Wang (2003), Coupled dynamics over the Indian Ocean: Spring initiation of the Zonal Mode, *Deep Sea Res., Part II*, *50*(12–13), 2305–2330, doi:10.1016/S0967-0645(03)00058-4.

Behera, S. S. K., J. J. J. Luo, S. Masson, S. A. Rao, H. Sakuma, and T. Yamagata (2006), A CGCM study on the interaction between IOD and ENSO, *J. Clim.*, *19*, 1688–1705, doi:10.1175/JCLI3797.1.

Bellon, G., A. H. Sobel, and J. Vialard (2008), Ocean-atmosphere coupling in the monsoon intraseasonal oscillation: A simple model study, *J. Clim.*, *21*(20), 5254–5270, doi:10.1175/2008JCLI2305.1.

Bender, M. A., and I. Ginis (2000), Real-case simulations of Hurricane–Ocean interaction using a high-resolution coupled model: Effects on Hurricane intensity, *Mon. Weather Rev.*, *128*(4), 917–946, doi:10.1175/1520-0493(2000)128<0917:RCSOHO>2.0.CO;2.
Bengtsson, L., M. Botzet, and M. Esch (1996), Will greenhouse gas-induced warming over the next 50 years lead to higher frequency and greater intensity of hurricanes?, *Tellus, Ser. A*, *48*, 57–73, doi:10.1034/j.1600-0870.1996.00004.x.
Betts, A. K. (1986), A new convective adjustment scheme. Part I: Observational and theoretical basis, *Q. J. R. Meteorol. Soc.*, *112*(473), 677–691, doi:10.1002/qj.49711247307.
Blanke, B., and P. Delecluse (1993), Variability of the tropical Atlantic Ocean simulated by a general circulation model with two different mixed-layer physics, *J. Phys. Oceanogr.*, *23*(7), 1363–1388, doi:10.1175/1520-0485(1993)023<1363:VOTTAO>2.0.CO;2.
Brodeau, L., B. Barnier, A.-M. Treguier, T. Penduff, and S. Gulev (2010), An ERA40-based atmospheric forcing for global ocean circulation models, *Ocean Model.*, *31*(3–4), 88–104, doi:10.1016/j.ocemod.2009.10.005.
Camargo, S., A. Barnston, and S. Zebiak (2005), A statistical assessment of tropical cyclone activity in atmospheric general circulation models, *Tellus, Ser. A*, *57*, 589–604.
Camargo, S. J., A. H. Sobel, A. G. Barnston, and K. A. Emanuel (2007), Tropical cyclone genesis potential index in climate models, *Tellus, Ser. A*, *59*(4), 428–443, doi:10.1111/j.1600-0870.2007.00238.x.
Chauvin, F., J.-F. Royer, and M. Déqué (2006), Response of hurricane-type vortices to global warming as simulated by ARPEGE-Climat at high resolution, *Clim. Dyn.*, *27*(4), 377–399, doi:10.1007/s00382-006-0135-7.
Chen, F., K. Mitchell, J. Schaake, Y. Xue, H.-L. Pan, V. Koren, Q. Y. Duan, M. Ek, and A. Betts (1996), Modeling of land surface evaporation by four schemes and comparison with FIFE observations, *J. Geophys. Res.*, *101*(D3), 7251–7268, doi:10.1029/95JD02165.
Chou, M., and M. Suarez (1999), A solar radiation parameterization for atmospheric studies, Tech Rep NASA/TM-1999-104606, NASA/GSFC.
Dash, S. K., M. S. Shekhar, and G. P. Singh (2006), Simulation of Indian summer monsoon circulation and rainfall using RegCM3, *Theor. Appl. Climatol.*, *86*(1–4), 161–172, doi:10.1007/s00704-006-0204-1.
de Boyer Montégut, C., J. Vialard, S. S. C. Shenoi, D. Shankar, F. Durand, C. Ethé, and G. Madec (2007), Simulated seasonal and interannual variability of the mixed layer heat budget in the Northern Indian Ocean, *J. Clim.*, *20*(13), 3249–3268, doi:10.1175/JCLI4148.1.
Dee, D. P., et al. (2011), The ERA-Interim reanalysis: Configuration and performance of the data assimilation system, *Q. J. R. Meteorol. Soc.*, *137*(656), 553–597, doi:10.1002/qj.828.
Deshpande, M., S. Pattnaik, and P. S. Salvekar (2010), Impact of physical parameterization schemes on numerical simulation of super cyclone Gonu, *Nat. Hazards*, *55*(2), 211–231, doi:10.1007/s11069-010-9521-x.
Donelan, M. A., B. K. Haus, N. Reul, W. J. Plant, M. Stiassnie, H. C. Graber, O. B. Brown, and E. S. Saltzman (2004), On the limiting aerodynamic roughness of the ocean in very strong winds, *Geophys. Res. Lett.*, *31*, L18306, doi:10.1029/2004GL019460.
Du, Y., S.-P. Xie, G. Huang, and K. Hu (2009), Role of air-sea interaction in the long persistence of El Niño-induced North Indian Ocean warming, *J. Clim.*, *22*(8), 2023–2038, doi:10.1175/2008JCLI2590.1.
Emanuel, K. A., and D. S. Nolan (2004), Tropical cyclone activity and the global climate system, Preprints, in *26th Conference on Hurricanes and Tropical Meteorology*, vol. *10*, pp. 240–241, Am. Meteorol. Soc., Boston, Mass.
Findlater, J. (1969), Interhemispheric transport of air in the lower troposphere over the western Indian Ocean, *Q. J. R. Meteorol. Soc.*, *95*(404), 400–403, doi:10.1002/qj.49709540412.
Fischer, A. S., P. Terray, E. Guilyardi, S. Gualdi, and P. Delecluse (2005), Two independent triggers for the Indian Ocean Dipole/Zonal Mode in a coupled GCM, *J. Clim.*, *18*(17), 3428–3449, doi:10.1175/JCLI3478.1.
Fu, X., and B. Wang (2004), Differences of boreal summer intraseasonal oscillations simulated in an atmosphere-ocean coupled model and an atmosphere-only model, *J. Clim.*, *17*(6), 1263–1271, doi:10.1175/1520-0442(2004)017<1263:DOBSIO>2.0.CO;2.
Gentry, M. S., and G. M. Lackmann (2010), Sensitivity of simulated tropical cyclone structure and intensity to horizontal resolution, *Mon. Weather Rev.*, *138*(3), 688–704, doi:10.1175/2009MWR2976.1.
Gomes, J. L., and S. C. Chou (2010), Dependence of partitioning of model implicit and explicit precipitation on horizontal resolution, *Meteorol. Atmos. Phys.*, *106*(1–2), 1–18, doi:10.1007/s00703-009-0050-7.
Goswami, B. N. (2005), South Asian Monsoon, in *Intraseasonal Variability in the Atmosphere-Ocean Climate System*, edited by W. K. M. Lau and D. E. Waliser, pp. 19–55, Springer, Berlin.
Graham, N. E., and T. P. Barnett (1987), Sea surface temperature, surface wind divergence, and convection over tropical oceans, *Science*, *238*(4827), 657–659, doi:10.1126/science.238.4827.657.
Hong, S.-Y., and J.-O. J. Lim (2006), The WRF Single-Moment 6-Class Microphysics Scheme (WSM6), *Asia-Pacific J. Atmos. Sci.*, *42*(2), 129–151.
Izumo, T., C. B. Montégut, J.-J. Luo, S. K. Behera, S. Masson, and T. Yamagata (2008), The role of the western Arabian Sea upwelling in Indian monsoon rainfall variability, *J. Clim.*, *21*(21), 5603–5623, doi:10.1175/2008JCLI2158.1.
Izumo, T., J. Vialard, M. Lengaigne, C. de Boyer Montegut, S. K. Behera, J.-J. Luo, S. Cravatte, S. Masson, and T. Yamagata (2010), Influence of the state of the Indian Ocean Dipole on the following year's El Niño, *Nat. Geosci.*, *3*(3), 168–172, doi:10.1038/ngeo760.
Janjić, Z. I. (1994), The step-mountain Eta coordinate model: Further developments of the convection, viscous sublayer, and turbulence closure schemes, *Mon. Weather Rev.*, *122*(5), 927–945, doi:10.1175/1520-0493(1994)122<0927:TSMECM>2.0.CO;2.
Janjić, Z. I. (2000), Comments on "Development and Evaluation of a Convection Scheme for Use in Climate Models," *J. Atmos. Sci.*, *57*(21), 3686–3686, doi:10.1175/1520-0469(2000)057<3686:CODAEO>2.0.CO;2.
Joseph, P. V., and S. Sijikumar (2004), Intraseasonal variability of the low-level jet stream of the Asian summer monsoon, *J. Clim.*, *17*(7), 1449–1458, doi:10.1175/1520-0442(2004)017<1449:IVOTLJ>2.0.CO;2.
Jourdain, N. C., P. Marchesiello, C. E. Menkes, J. Lefèvre, E. M. Vincent, M. Lengaigne, and F. Chauvin (2011), Mesoscale simulation of tropical cyclones in the South Pacific: Climatology and interannual variability, *J. Clim.*, *24*(1), 3–25, doi:10.1175/2010JCLI3559.1.
Jourdain, N. C., B. Barnier, N. Ferry, J. Vialard, C. E. Menkes, M. Lengaigne, and L. Parent (2014), Tropical cyclones in two atmospheric (re)analyses and their response in two oceanic reanalyses, *Ocean Modell.*, *73*, 108–122, doi:10.1016/j.ocemod.2013.10.007.
Jullien, J., P. Marchesiello, C. E. Menkes, J. Lefèvre, N. C. Jourdain, G. Samson, and M. Lengaigne (2014), Ocean feedback to tropical cyclones: Climatology and processes, *Clim. Dyn.*, 1–24, doi:10.1007/s00382-014-2096-6.
Kain, J. S. (2004), The Kain-Fritsch convective parameterization: An update, *J. Appl. Meteorol.*, *43*(1), 170–181, doi:10.1175/1520-0450(2004)043<0170:TKCPAU>2.0.CO;2.
Kain, J. S., and M. J. Fritsch (1993), Convective parameterization for mesoscale models: The Kain-Fritsch scheme, in *The Representation of Cumulus Convection in Numerical Models, Meteorol. Monogr.*, vol. *46*, edited by K. A. Emanuel and D. J. Raymond, pp. 165–170, Am. Meteorol. Soc., Boston, Mass.
Keerthi, M. G., M. Lengaigne, J. Vialard, C. Boyer Montégut, and P. M. Muraleedharan (2012), Interannual variability of the tropical Indian Ocean mixed layer depth, *Clim. Dyn.*, *40*(3–4), 743–759, doi:10.1007/s00382-012-1295-2.

Kitoh, A., and S. Kusunoki (2007), East Asian summer monsoon simulation by a 20-km mesh AGCM, *Clim. Dyn.*, *31*(4), 389–401, doi:10.1007/s00382-007-0285-2.
Klein, S. A., B. J. Soden, and N.-C. Lau (1999), Remote sea surface temperature variations during ENSO: Evidence for a tropical atmospheric bridge, *J. Clim.*, *12*(4), 917–932, doi:10.1175/1520-0442(1999)012<0917:RSSTVD>2.0.CO;2.
Klingaman, N. P., S. J. Woolnough, H. Weller, and J. M. Slingo (2011), The impact of finer-resolution air-sea coupling on the intraseasonal oscillation of the Indian monsoon, *J. Clim.*, *24*(10), 2451–2468, doi:10.1175/2010JCLI3868.1.
Knapp, K. R., M. C. Kruk, D. H. Levinson, H. J. Diamond, and C. J. Neumann (2010), The International Best Track Archive for Climate Stewardship (IBTrACS), *Bull. Am. Meteorol. Soc.*, *91*(3), 363–376, doi:10.1175/2009BAMS2755.1.
Knutson, T. R., J. J. Sirutis, S. T. Garner, I. M. Held, and R. E. Tuleya (2007), Simulation of the recent multidecadal increase of Atlantic hurricane activity using an 18-km-grid regional model, *Bull. Am. Meteorol. Soc.*, *88*(10), 1549–1565, doi:10.1175/BAMS-88-10-1549.
Krishna Kumar, K. (2005), Advancing dynamical prediction of Indian monsoon rainfall, *Geophys. Res. Lett.*, *32*, L08704, doi:10.1029/2004GL021979.
Krishna Kumar, K. K. (1999), On the weakening relationship between the Indian monsoon and ENSO, *Science*, *284*(5423), 2156–2159, doi:10.1126/science.284.5423.2156.
Kumar, B. P., J. Vialard, M. Lengaigne, V. S. N. Murty, G. R. Foltz, M. J. McPhaden, S. Pous, and C. Boyer Montégut (2014), Processes of interannual mixed layer temperature variability in the thermocline ridge of the Indian Ocean, *Clim. Dyn.*, 1–21, doi:10.1007/s00382-014-2059-y.
Kurian, N., M. Lengaigne, G. V. Vissa, J. Vialard, S. Pous, A.-C. Peter, F. Durand, and S. Naik (2013), Processes of India's offshore summer intraseasonal sea surface temperature variability, *Ocean Dyn.*, *63*(4), 329–346, doi:10.1007/s10236-013-0604-6.
Landman, W., A. Seth, and S. Camargo (2005), The effect of regional climate model domain choice on the simulation of tropical cyclone-like vortices in the Southwestern Indian Ocean, *J. Clim.*, *18*(8), 1263–1274.
Lengaigne, M., G. Madec, C. E. Menkes, and G. Alory (2003), Impact of isopycnal mixing on the tropical ocean circulation, *J. Geophys. Res.*, *108*(C11), 3345, doi:10.1029/2002JC001704.
Lengaigne, M., U. Hausmann, G. Madec, C. Menkes, J. Vialard, and J. M. Molines (2011), Mechanisms controlling warm water volume interannual variations in the equatorial Pacific: Diabatic versus adiabatic processes, *Clim. Dyn.*, *38*(5–6), 1031–1046, doi:10.1007/s00382-011-1051-z.
Leung, L. R., Y.-H. Kuo, and J. Tribbia (2006), Research needs and directions of regional climate modeling using WRF and CCSM, *Bull. Am. Meteorol. Soc.*, *87*(12), 1747–1751, doi:10.1175/BAMS-87-12-1747.
Longshore, D. (2009), *Encyclopedia of Hurricanes, Typhoons, and Cyclones*, Infobase Publishing, New York.
Lucas-Picher, P., J. H. Christensen, F. Saeed, P. Kumar, S. Asharaf, B. Ahrens, A. J. Wiltshire, D. Jacob, and S. Hagemann (2011), Can regional climate models represent the Indian monsoon?, *J. Hydrometeorol.*, *12*(5), 849–868, doi:10.1175/2011JHM1327.1.
Madec, G. (2008), NEMO ocean engine, *Notes du Pole de Modelisation 27*, Inst. Pierre-Simon Laplace, Paris, France.
McCreary, J. P., P. K. Kundu, and R. L. Molinari (1993), A numerical investigation of dynamics, thermodynamics and mixed-layer processes in the Indian Ocean, *Prog. Oceanogr.*, *31*(3), 181–244, doi:10.1016/0079-6611(93)90002-U.
McPhaden, M. J., S. E. Zebiak, and M. H. Glantz (2006), ENSO as an integrating concept in earth science, *Science*, *314*(5806), 1740–1745, doi:10.1126/science.1132588.
Menkes, C. E., M. Lengaigne, P. Marchesiello, N. C. Jourdain, E. M. Vincent, J. Lefèvre, F. Chauvin, and J.-F. Royer (2011), Comparison of tropical cyclogenesis indices on seasonal to interannual timescales, *Clim. Dyn.*, *38*(1–2), 301–321, doi:10.1007/s00382-011-1126-x.
Mlawer, E. J., S. J. Taubman, P. D. Brown, M. J. Iacono, and S. A. Clough (1997), Radiative transfer for inhomogeneous atmospheres: RRTM, a validated correlated-k model for the longwave, *J. Geophys. Res.*, *102*(D14), 16,663–16,682, doi:10.1029/97JD00237.
Mukhopadhyay, P., S. Taraphdar, B. N. Goswami, and K. Krishnakumar (2010), Indian summer monsoon precipitation climatology in a high-resolution regional climate model: Impacts of convective parameterization on systematic biases, *Weather Forecasting*, *25*(2), 369–387, doi:10.1175/2009WAF2222320.1.
Murakami, H., and B. Wang (2010), Future change of North Atlantic tropical cyclone tracks: Projection by a 20-km-mesh global atmospheric model, *J. Clim.*, *23*(10), 2699–2721, doi:10.1175/2010JCLI3338.1.
Neetu, S., M. Lengaigne, E. M. Vincent, J. Vialard, G. Madec, G. Samson, M. R. Ramesh Kumar, and F. Durand (2012), Influence of upper-ocean stratification on tropical cyclone-induced surface cooling in the Bay of Bengal, *J. Geophys. Res.*, *117*, C12020, doi:10.1029/2012JC008433.
Nidheesh, A. G., M. Lengaigne, J. Vialard, A. S. Unnikrishnan, and H. Dayan (2012), Decadal and long-term sea level variability in the tropical Indo-Pacific Ocean, *Clim. Dyn.*, *41*(2), 381–402, doi:10.1007/s00382-012-1463-4.
Noh, Y., W. G. Cheon, S. Y. Hong, and S. Raasch (2003), Improvement of the K-profile model for the planetary boundary layer based on large eddy simulation data, *Boundary Layer Meteorol.*, *107*(2), 401–427, doi:10.1023/A:1022146015946.
Price, J. F. (1981), Upper ocean response to a hurricane, *J. Phys. Oceanogr.*, *11*(2), 153–175, doi:10.1175/1520-0485(1981)011<0153:UORTAH>2.0.CO;2.
Ratnam, J. V., and K. K. Kumar (2005), Sensitivity of the simulated monsoons of 1987 and 1988 to convective parameterization schemes in MM5, *J. Clim.*, *18*(14), 2724–2743, doi:10.1175/JCLI3390.1.
Ratnam, J. V., F. Giorgi, A. Kaginalkar, and S. Cozzini (2008), Simulation of the Indian monsoon using the RegCM3-ROMS regional coupled model, *Clim. Dyn.*, *33*(1), 119–139, doi:10.1007/s00382-008-0433-3.
Saji, N. H., B. N. Goswami, P. N. Vinayachandran, and T. Yamagata (1999), A dipole mode in the tropical Indian Ocean, *Nature*, *401*(6751), 360–363.
Samala, B. K., N. C. S. Banerjee, A. Kaginalkar, and M. Dalvi (2013), Study of the Indian summer monsoon using WRF-ROMS regional coupled model simulations, *Atmos. Sci. Lett.*, *14*(1), 20–27, doi:10.1002/asl2.409.
Satoh, M. et al. (2011), The intra-seasonal oscillation and its control of tropical cyclones simulated by high-resolution global atmospheric models, *Clim. Dyn.*, *39*(9–10), 2185–2206, doi:10.1007/s00382-011-1235-6.
Schade, L. R. (2000), Tropical cyclone intensity and sea surface temperature, *J. Atmos. Sci.*, *57*(18), 3122–3130, doi:10.1175/1520-0469(2000)057<3122:TCIASS>2.0.CO;2.
Schade, L. R., and K. A. Emanuel (1999), The Ocean's effect on the intensity of tropical cyclones: Results from a simple coupled atmosphere-ocean model, *J. Atmos. Sci.*, *56*(4), 642–651, doi:10.1175/1520-0469(1999)056<0642:TOSEOT>2.0.CO;2.
Schott, F. A., S.-P. Xie, and J. P. McCreary (2009), Indian Ocean circulation and climate variability, *Rev. Geophys.*, *47*, RG1002, doi:10.1029/2007RG000245.
Seo, H., R. Murtugudde, M. Jochum, and A. J. Miller (2008), Modeling of mesoscale coupled ocean-atmosphere interaction and its feedback to ocean in the western Arabian Sea, *Ocean Modell.*, *25*(3–4), 120–131, doi:10.1016/j.ocemod.2008.07.003.

Seo, H., S.-P. Xie, R. Murtugudde, M. Jochum, and A. J. Miller (2009), Seasonal effects of Indian Ocean freshwater forcing in a regional coupled model, *J. Clim.*, *22*(24), 6577–6596, doi:10.1175/2009JCLI2990.1.

Skamarock, W. C., and J. B. Klemp (2008), A time-split nonhydrostatic atmospheric model for weather research and forecasting applications, *J. Comput. Phys.*, *227*(7), 3465–3485, doi:10.1016/j.jcp.2007.01.037.

Sperber, K. R., H. Annamalai, I.-S. Kang, A. Kitoh, A. Moise, A. Turner, B. Wang, and T. Zhou (2012), The Asian summer monsoon: An intercomparison of CMIP5 vs. CMIP3 simulations of the late 20th century, *Clim. Dyn.*, *41*(9–10), 2711–2744, doi:10.1007/s00382-012-1607-6.

Srinivas, C. V., R. Venkatesan, D. V. B. Rao, and D. H. Prasad (2007), Numerical simulation of Andhra Severe Cyclone (2003): Model sensitivity to the boundary layer and convection parameterization, in *Atmospheric and Oceanic Mesoscale Processes*, edited by M. Sharan and S. Raman, pp. 1465–1487, Birkhäuser, Basel, Switzerland.

Srinivas, C. V., D. Hariprasad, D. V. Bhaskar Rao, Y. Anjaneyulu, R. Baskaran, and B. Venkatraman (2013a), Simulation of the Indian summer monsoon regional climate using advanced research WRF model, *Int. J. Climatol.*, *33*(5), 1195–1210, doi:10.1002/joc.3505.

Srinivas, C. V., D. V. Bhaskar Rao, V. Yesubabu, R. Baskaran, and B. Venkatraman (2013b), Tropical cyclone predictions over the Bay of Bengal using the high-resolution Advanced Research Weather Research and Forecasting (ARW) model, *Q. J. R. Meteorol. Soc.*, *139*(676), 1810–1825, doi:10.1002/qj.2064.

Strachan, J., P. L. Vidale, K. Hodges, M. Roberts, and M.-E. Demory (2013), Investigating global tropical cyclone activity with a hierarchy of AGCMs: The role of model resolution, *J. Clim.*, *26*(1), 133–152, doi:10.1175/JCLI-D-12-00012.1.

Tippett, M. K., S. J. Camargo, and A. H. Sobel (2011), A Poisson regression index for tropical cyclone genesis and the role of large-scale vorticity in genesis, *J. Clim.*, *24*(9), 2335–2357, doi:10.1175/2010JCLI3811.1.

Treguier, A. M., B. Barnier, A. P. de Miranda, J. M. Molines, N. Grima, M. Imbard, G. Madec, C. Messager, T. Reynaud, and S. Michel (2001), An eddy-permitting model of the Atlantic circulation: Evaluating open boundary conditions, *J. Geophys. Res.*, *106*(C10), 22,115–22,129, doi:10.1029/2000JC000376.

Tuleya, R. E., M. DeMaria, and R. J. Kuligowski (2007), Evaluation of GFDL and simple statistical model rainfall forecasts for U.S. landfalling tropical storms, *Weather Forecasting*, *22*, 56–70, doi:10.1175/WAF972.1.

Turner, A. G., and H. Annamalai (2012), Climate change and the South Asian summer monsoon, *Nat. Clim. Change*, *2*(8), 587–595, doi:10.1038/nclimate1495.

Vaidya, S. S., and S. S. Singh (2000), Applying the Betts-Miller-Janjic scheme of convection in prediction of the Indian monsoon, *Weather Forecasting*, *15*(3), 349–356, doi:10.1175/1520-0434(2000)015<0349:ATBMJS>2.0.CO;2.

Valcke, S. (2013), The OASIS3 coupler: A European climate modelling community software, *Geosci. Model Dev.*, *6*(2), 373–388, doi:10.5194/gmd-6-373-2013.

Vecchi, G. A., and D. E. Harrison (2002), Monsoon breaks and subseasonal sea surface temperature variability in the Bay of Bengal, *J. Clim.*, *15*(12), 1485–1493, doi:10.1175/1520-0442(2002)015<1485:MBASSS>2.0.CO;2.

Vialard, J., A. Jayakumar, C. Gnanaseelan, M. Lengaigne, D. Sengupta, and B. N. Goswami (2011), Processes of 30–90 days sea surface temperature variability in the northern Indian Ocean during boreal summer, *Clim. Dyn.*, *38*(9–10), 1901–1916, doi:10.1007/s00382-011-1015-3.

Vialard, J., K. Drushka, H. Bellenger, M. Lengaigne, S. Pous, and J. P. Duvel (2012), Understanding Madden-Julian-Induced sea surface temperature variations in the North Western Australian Basin, *Clim. Dyn.*, *41*(11–12), 3203–3218, doi:10.1007/s00382-012-1541-7.

Vincent, E. M., M. Lengaigne, G. Madec, J. Vialard, G. Samson, N. C. Jourdain, C. E. Menkes, and S. Jullien (2012), Processes setting the characteristics of sea surface cooling induced by tropical cyclones, *J. Geophys. Res.*, *117*, C02020, doi:10.1029/2011JC007396.

Vitart, F., J. L. Anderson, and W. F. Stern (1997), Simulation of interannual variability of tropical storm frequency in an ensemble of GCM integrations, *J. Clim.*, *10*(4), 745–760, doi:10.1175/1520-0442(1997)010<0745:SOIVOT>2.0.CO;2.

Walsh, K. J. E., M. Fiorino, C. W. Landsea, and K. L. McInnes (2007), Objectively determined resolution-dependent threshold criteria for the detection of tropical cyclones in climate models and reanalyses, *J. Clim.*, *20*(10), 2307–2314, doi:10.1175/JCLI4074.1.

Wang, B., Q. Ding, X. Fu, I.-S. Kang, K. Jin, J. Shukla, and F. Doblas-Reyes (2005), Fundamental challenge in simulation and prediction of summer monsoon rainfall, *Geophys. Res. Lett.*, *32*, L15711, doi:10.1029/2005GL022734.

Wang, Y., L. R. Leung, J. L. McGregor, D.-K. Lee, W.-C. Wang, Y. Ding, and F. Kimura (2004), Regional climate modeling: Progress, challenges, and prospects, *J. Meteorol. Soc. Jpn.*, *82*(6), 1599–1628, doi:10.2151/jmsj.82.1599.

Webster, P. J., A. M. Moore, J. P. Loschnigg, and R. R. Leben (1999), Coupled ocean-atmosphere dynamics in the Indian Ocean during 1997–98, *Nature*, *401*(6751), 356–60, doi:10.1038/43848.

Willoughby, H. E., R. W. R. Darling, and M. E. Rahn (2006), Parametric representation of the primary hurricane vortex. Part II: A new family of sectionally continuous profiles, *Mon. Weather Rev.*, *134*(4), 1102–1120, doi:10.1175/MWR3106.1.

Wu, R., and B. P. Kirtman (2004), Impacts of the Indian Ocean on the Indian summer monsoon–ENSO relationship, *J. Clim.*, *17*(15), 3037–3054, doi:10.1175/1520-0442(2004)017<3037:IOTIOO>2.0.CO;2.

Xie, S.-P., H. Annamalai, F. A. Schott, and J. P. McCreary (2002), Structure and mechanisms of South Indian Ocean climate variability, *J. Clim.*, *15*(8), 864–878, doi:10.1175/1520-0442(2002)015<0864:SAMOSI>2.0.CO;2.

Xie, S.-P., K. Hu, J. Hafner, H. Tokinaga, Y. Du, G. Huang, and T. Sampe (2009), Indian Ocean capacitor effect on Indo-Western Pacific climate during the summer following El Niño, *J. Clim.*, *22*(3), 730–747, doi:10.1175/2008JCLI2544.1.

Yamagata, T., S. K. Behera, J.-J. Luo, S. Masson, M. R. Jury, and S. A. Rao (2004), Coupled ocean-atmosphere variability, in *Earth's Climate: The Ocean-Atmosphere Interaction*, vol. *147*, edited by C. Wang, S.-P. Xie, and J. A. Carton, AGU, Washington, D. C., doi: 10.1029/147GM12.

Yang, B., Y. Qian, G. Lin, R. Leung, and Y. Zhang (2012), Some issues in uncertainty quantification and parameter tuning: A case study of convective parameterization scheme in the WRF regional climate model, *Atmos. Chem. Phys.*, *12*(5), 2409–2427, doi:10.5194/acp-12-2409-2012.

Zhao, M., I. M. Held, S.-J. Lin, and G. A. Vecchi (2010), Simulations of global hurricane climatology, interannual variability, and response to global warming using a 50-km resolution GCM, *J. Clim.*, *22*, 6653–6678.

Zou, L., and T. Zhou (2011), Development and evaluation of a regional ocean-atmosphere coupled model with focus on the western North Pacific summer monsoon simulation: Impacts of different atmospheric components, *Sci. China Earth Sci.*, *55*(5), 802–815, doi:10.1007/s11430-011-4281-3.